NTNU

Norwegian University of
Science and Technology

# Fabrication and characterization of optical waveguide components in epitaxial (Pb,La)(Zr,Ti)O3 thin films.

**Jon Øyvind Kjellman**

Master of Science in Electronics
Submission date: June 2009
Supervisor: Jostein Grepstad, IET

Norwegian University of Science and Technology
Department of Electronics and Telecommunications

# Problem Description

The ferroelectric perovskite PLZT (i.e., (Pb,La)(Zr,Ti)O3) is recognized as an attractive material for electrically controllable optical devices, by virtue of its strong electro-optic response and low propagation losses at visible and infrared wavelengths. The electro-optic response may be "linear" (Pockels effect) or "quadratic" (Kerr effect) dependent on the PLZT cation stoichiometry, the former being a prerequisite for application in phase and intensity modulators, as well as in electro-optic switches.

In this project, we intend to investigate the electro-optic characteristics of PLZT thin films grown epitaxially by magnetron sputter deposition in the Oxide Electronics Lab @ IET (http://www.iet.ntnu.no/en/groups/material_og_komponent/oxide_electronics_research). The experimental work will involve processing of ridge-type optical waveguides and Mach-Zehnder type electro-optic modulators in such thin films using standard UV lithography and wet-etching techniques. An experimental setup using tapered optical fibers to couple light into these thin film waveguides will be used for optical characterization of both device and the PLZT thin film material.

Assignment given: 15. January 2009
Supervisor: Jostein Grepstad, IET

## Preface

This master thesis presents the work performed by me between January 2009 and June 2009. It is the final part of the degree requirements for my MSc in Electronics at the Norwegian University of Science and Technology (NTNU). The problem has been given by professor Jostein Grepstad and the work has been supervised by PhD research fellow Ørnulf Nordseth, both of whom have been of great help. I would also like to thank SINTEF for lending me their NIR camera and waveguide masks, PhD research fellow Chang Chuan You for performing AFM and PFM measurements and Erlend Furuset Jensen for linguistic assistance.

Jon Øyvind Kjellman

**Abstract**

This report presents a method for fabrication of ridge-type waveguide electro-optic modulators in 500 nm thick, *c*-oriented, epitaxial, $(Pb_{0.92},La_{0.08})(Zr_{0.4},Ti_{0.6})O_3$ thin films on a MgO substrate. The method is based on ordinary photolitography and wet etching techniques with lift-off metallisation of gold electrodes. To achieve good input coupling of light the device end faces were polished using diamond lapping films with grain sizes as small as 0.5 μm. Several devices with both Mach-Zehnder electro-optic modulators and phase modulators with co-planar gold electrodes and an interaction length of $L = 3$ mm were fabricated using this method. These modulators were used to examine the electro-optic effect in the thin film at the wavelength $\lambda = 1.55$ μm. Coherent, linearly polarised light was coupled into the waveguide end face using tapered fibres while a modulation voltage was applied to the electrodes. The phase modulators were used as intensity modulators by exciting them with light polarised 45° on the optical axis and placing a linear polariser at the output.

Practical modulation was achieved using voltages as low as 46 V with the phase modulators and 80 V with the Mach-Zehnder modulators. Using a numerical curve fitting technique, the measured data was fitted to a proposed theoretical model for the modulators. The model was based on Jones matrix formalism and the assumption that the electro-optic effect in the thin films corresponds with the Pockels effect. Good fits were achieved indicating that the effect is indeed a Pockels effect and estimates of the Pockels coefficient $\mathfrak{r}_{51}$ ranged from 4.4 pm/V to 11 pm/V depending on the device. These values were obtained under the uncertain assumption that the birefringence of (Pb,La)(Zr,Ti)$O_3$ is $\Delta n \approx 0.005$. It is found that if the actual value of $\Delta n$ be lower, then $\mathfrak{r}_{51}$ will also be lower than estimated.

Based on previous works the Pockels coefficient was expected to be on the order or $\sim 10^2$ pm/V. The low measured values of $\mathfrak{r}_{51}$ and the variation between films is believed to be due to the thin film being multi domain with a domain structure created by a stochastic process.

# Contents

# List of Figures

# List of Tables

## Acronyms

**AFM** atomic force microscopy

**DI** de-ionised

**DUT** device under test

**EBPVD** electron beam physical vapour deposition

**FPC** fibre polarisation-controller

**HMDS** hexamethyldisilazane

**IPA** isopropanol

**MgO** magnesium oxide

**MZI** Mach-Zehnder interferometer

**MZEOM** Mach-Zehnder electro-optic modulator

**NIR** near infrared

**PBS** polarising beam-splitter

**PFM** piezo force microscopy

**PLZT** (Pb,La)(Zr,Ti)$O_3$

**PM** phase modulator

**PZT** Pb(Zr,Ti)$O_3$

**TE** transverse electric (wave)

**TEM** transverse electromagnetic (wave)

**TM** transverse magnetic (wave)

**UV** ultra violet (light)

# 1 Introduction

The ceramic perovskite (Pb,La)(Zr,Ti)$O_3$ (PLZT) has attracted much interest due to its functional properties, such as piezo-, pyro- and ferro-electricity. A strong linear electro-optic response with a Pockels coefficient as large as $\sim 10^2$ pm/V has been reported for PLZT [1]. Epitaxial PLZT thin films grown on magnesium oxide (MgO) substrate have high crystalline quality and the thin film/substrate combination provides excellent index contrast, enabling the creation of strongly guiding waveguides to be fabricated [2]. These properties, combined with high transparency at visible and near-infrared wavelengths make PLZT an interesting material for developing highly integrated electro-optic devices with low operating voltages.

The goal of this work is to determine if practical electro-optic modulators with a co-planar electrode structure can be fabricated in epitaxial *c*-oriented PLZT thin films on MgO substrate. It is then desirable to examine the electro-optic response of both Mach-Zehnder type electro-optic modulators and phase modulators. Using Jones matrix formalisms, a model for both Mach-Zehnder electro-optic modulators and phase modulators will be proposed. By fitting the measured values to the proposed model it is desirable to arrive at an approximate value for the fundamental value of the $\mathfrak{r}_{51}$ Pockels coefficient of the PLZT thin film. By knowing the exact value of $\mathfrak{r}_{51}$, better simulations of the electro-optic effect are facilitated; increasing the precision of the design of new electro-optic devices in PLZT thin films by reducing the number of unknown factors.

This report will start with proposing a theoretical model for the modulators in section 2 before fabrication and the expreimental setup is discussed in section 3, section 4 and section 5. The results will then be presented and discussed in section 6. The report is concluded in section 7. The following section 8 suggests areas of future research related to ridge-type waveguide electro-optic modulators in PLZT thin films.

# 2 Theory and numerical simulations

In order to support the analysis of the obtained results, this chapter will present supporting theory and numerical simulations of the ridge-type waveguide structure with co-planar electrodes. Numerical simulations for calculating the mode profiles were performed using FIMMWAVE version 4.6 while system simulations have been performed using a number of custom scripts for MATLAB version 7.7.0.

## 2.1 Thin film structure

The composition of the PLZT thin film that is applied for this project is 8/40/60 (ie, $(Pb_{0.92},La_{0.08})(Zr_{0.4},Ti_{0.6})O_3$) and it is $c$-oriented with a tetragonal perovskite structure [2]. This means that in the tetragonal unit cell where $\boldsymbol{a} \perp \boldsymbol{b} \perp \boldsymbol{c}$ and $a = b \neq c$, the $c$-axis is directed perpendicular to the film plane. A consistent notation has been adopted for this report where the $xyz$-coordinate system is parallel to the $abc$-coordinate system.

## 2.2 Basic properties of the ridge-type waveguide

The ridge-type optical waveguide is a practical waveguide which is simple to manufacture; using a common photolitography process it can be created with a single etch, requiring only one mask and one exposure. The ridge-type waveguide has also got excellent confinement which reduces losses from surface scattering.

The geometry of the ridge-type waveguide is shown in figure 2.1 and it is defined by the ridge width $W$, film thickness $h_f$ and etch depth $h$. For this project the film thickness is always assumed to be $h_f = 500$ nm.

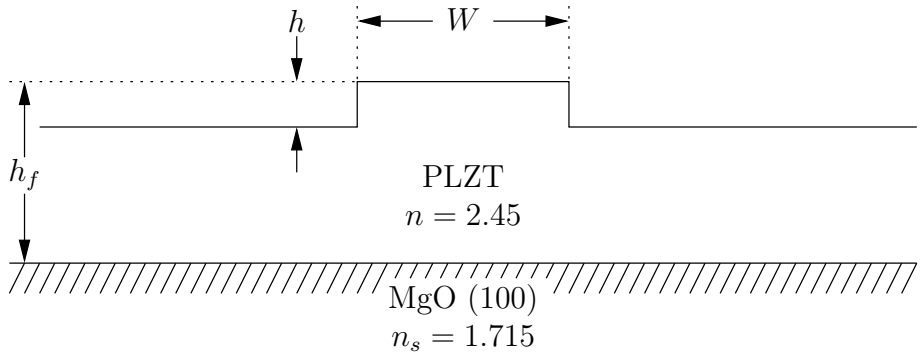


Figure 2.1: Cross section of ridge-type waveguide in PLZT thin film on MgO substrate.

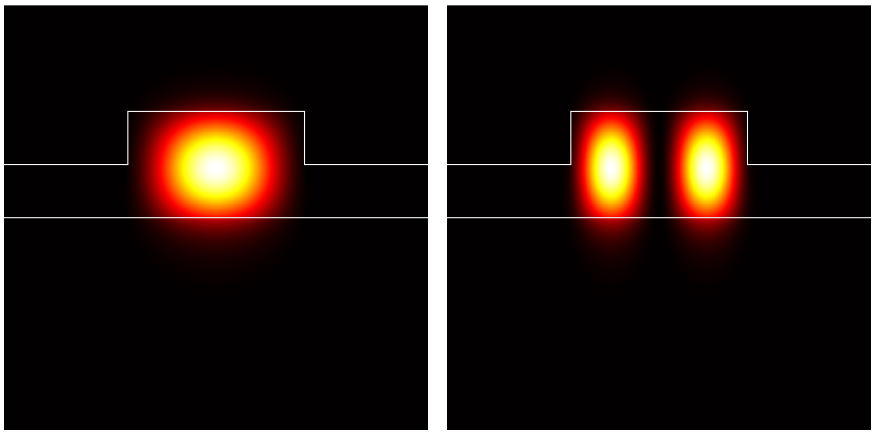

(a) $TE_0$ (b) $TE_1$

Figure 2.2: Intensity distribution in the $TE_0$ and $TE_1$ mode for an arbitrary ridge-type waveguide.

Simulations using FIMMWAVE shows that the ridge type waveguide supports both transverse electric (TE) and transverse magnetic (TM) modes. The electric field of the different modes is either symmetrical or anti symmetrical around the $z$-axis. Due to symmetry, the $E$-field must be directed along the $x$-axis in the case of TE modes. For TM modes, the $H$-field must be directed along the $x$-axis and as a consequence it is reasonable to assume that the $E$-field will be directed along the $z$-axis—at least on average. The modes are denoted $TE_m$ or $TM_m$ where $m \in \mathbb{N}$ is the mode order. In general, the field will have $m+1$ extremes along the horizontal axis. For every possible waveguide geometry there exists an upper limit to m. Figure 2.2 illustrates how the intensity is distributed in the first two modes of an arbitrary ridge-type waveguide. The $TM_0$ and $TM_1$ modes will in general have a similar intensity distribution, though simulations show that they will be slightly less well confined compared to the TE modes.

## 2.3 Electro optic effect in PLZT

When an electric field is applied to a material which exhibits electro-optic effect, the refractive index $n$ is modified. For a slowly varying applied electric field $E$, this effect can be written as a Taylor expansion

$$n(E) = n_0 + a_1 E + \frac{1}{2} a_2 E^2 + ... \tag{2.1}$$

where $n_0$ is the unperturbed refractive index and $a_i = \mathrm{d}^i n / \mathrm{d}E^i \big|_{E=0}$ are the expansion coefficients. The terms higher than the second order term of this expansion are in many materials such as PLZT weak compared to the second

order term and thus neglected. As a result the electro-optic effect in PLZT can be described by

$$n(E) \approx n - \frac{1}{2}\mathfrak{r}\, n^3 E \tag{2.2}$$

where $\mathfrak{r} = -2a_1/n^3$ is referred to as the Pockels coefficient. However, for anisotropic materials such as PLZT, the electro-optical effect perturbs the index ellipsoid. Using Einstein notation, the impermeability tensor $\eta$ is then perturbed according to (2.3) [3] where $i, j, k \in \{1, 2, 3\}$ are coordinate indices corresponding to the $x$-, $y$-, and $z$ axis, respectively.

$$\eta_{ij} = \eta_{ij}(0) + \mathfrak{r}_{ijk} E_k \tag{2.3}$$

For a co-planar electrode geometry the static electric field below the waveguide ridge will be approximately horizontal; this is confirmed by simulations of a DC electric field in FIMMWAVE. Expressed mathematically, the applied electric field can be approximated as

$$E_k \approx \begin{cases} \frac{V}{d} & \text{for} \quad k = 1 \\ 0 & \text{for} \quad k \in \{2, 3\} \end{cases} \tag{2.4}$$

where $d$ is the waveguide gap. However, there will not be complete overlap between the optic field and the applied electric field in the thin film. Part of the optic field will propagate in the substrate below and air above, which are both assumed to not exhibit any electro-optic effect. This can be corrected by using

$$E_k \approx \begin{cases} \frac{V}{d}\Gamma & \text{for} \quad k = 1 \\ 0 & \text{for} \quad k \in \{2, 3\} \end{cases} \tag{2.5}$$

which is suggested by [4] as a better approximation. Here $\Gamma$ is an overlap factor which is defined as

$$\Gamma = \frac{d}{V} \iint_A E_1 |E_{o,n}|^2 \mathrm{d}A, \tag{2.6}$$

where $E_{o,n}$ is the normalized optical field, $E_1$ is the actual static field and $A$ is the entire cross sectional area. Given that PLZT is an anisotropic material it is not obvious that it is the $E_1$ component that should be used in (2.6), but it seems reasonable to assume that the electro-optic effect induced by the vertical components is small with co-planar electrodes sufficiently removed from the optical field. Since the mode is well confined in the thin-film below the ridge, little of the optical field extends below the electrodes where the DC-field becomes vertical. Thus, $\Gamma$ has been estimated for the fundamental mode by calculating the total power confined in the entire thin-film divided by the total power in the whole cross section using FIMMWAVE's *fillfactor* parameter. A slight difference in $\Gamma$ between the $TE_0$ and $TM_0$ modes is

found, but this difference is ignored in order to simplify the analysis. The estimated value is $\Gamma \approx 0.88$.

It has been established that there are several phases of PLZT with different crystal symmetries [1]. As previously mentioned, the 8/40/60 PLZT that was used for this project has a tetragonal perovskite structure, and thus belongs to the 4mm point group [1]. The Pockels tensor for the 4mm point group is given by [5] as

$$\mathfrak{r} = \begin{pmatrix} 0 & 0 & \mathfrak{r}_{13} \\ 0 & 0 & \mathfrak{r}_{13} \\ 0 & 0 & \mathfrak{r}_{33} \\ 0 & \mathfrak{r}_{51} & 0 \\ \mathfrak{r}_{51} & 0 & 0 \\ 0 & 0 & 0 \end{pmatrix}. \tag{2.7}$$

8/40/60 PLZT is also an uniaxial crystal giving the unperturbed impermeability tensor as

$$\eta(0) = \begin{pmatrix} \frac{1}{n_o^2} & 0 & 0 \\ 0 & \frac{1}{n_o^2} & 0 \\ 0 & 0 & \frac{1}{n_e^2} \end{pmatrix}, \tag{2.8}$$

where $n_o$ is the ordinary refractive index and $n_e$ is the extraordinary refractive index.

Inserting (2.5), (2.7) and (2.8) into (2.3) gives the perturbed impermeability tensor.

$$\eta(V) = \begin{pmatrix} \frac{1}{n_o^2} & 0 & \mathfrak{r}_{51}\frac{V}{d}\Gamma \\ 0 & \frac{1}{n_o^2} & 0 \\ \mathfrak{r}_{51}\frac{V}{d}\Gamma & 0 & \frac{1}{n_e^2} \end{pmatrix}. \tag{2.9}$$

As shown in appendix A, this tensor can be diagonalised by a rotation around the $y$-axis. From (A.24), the diagonalised impermeability tensor can be written as

$$\eta' = \begin{pmatrix} \frac{1}{n_o^2} + \mathfrak{r}_{51}\frac{V}{d}\Gamma\tan\theta & 0 & 0 \\ 0 & \frac{1}{n_o^2} & 0 \\ 0 & 0 & \frac{1}{n_e^2} - \mathfrak{r}_{51}\frac{V}{d}\Gamma\tan\theta \end{pmatrix}. \tag{2.10}$$

where $\theta$ is the angle of rotation given by (A.20) which written out becomes

$$\theta = \arctan\left[\frac{1}{2\mathfrak{r}_{51}\frac{V}{d}\Gamma}\left(\frac{1}{n_e^2} - \frac{1}{n_o^2} + \sqrt{\left(\frac{1}{n_o^2} - \frac{1}{n_e^2}\right)^2 + 4\left(\mathfrak{r}_{51}\frac{V}{d}\Gamma\right)^2}\right)\right]. \tag{2.11}$$

From (2.11) it is possible to show that $\lim_{V\to\pm\infty}\tan\theta = \pm 1$ which implies that this the rotation tends towards $\pm 45°$ for high voltages. Figure 2.3 is a

plot of the $\theta$ on the vertical axis and the applied modulation voltage $V$ on the horizontal axis for a set of different $\mathfrak{r}_{51}$. The plot clearly shows the trend towards $\pm 45°$ with the curve for $\mathfrak{r}_{51} = 125$ pm/V. The figure also shows that $\theta$ is approximately linear for small voltages. From the figure, it is clear that what constitutes a large voltage increases for decreasing $\mathfrak{r}_{51}$. In other words, $\theta$ is approximately linear in a large region around $V = 0$ V for small values of $\mathfrak{r}_{51}$.

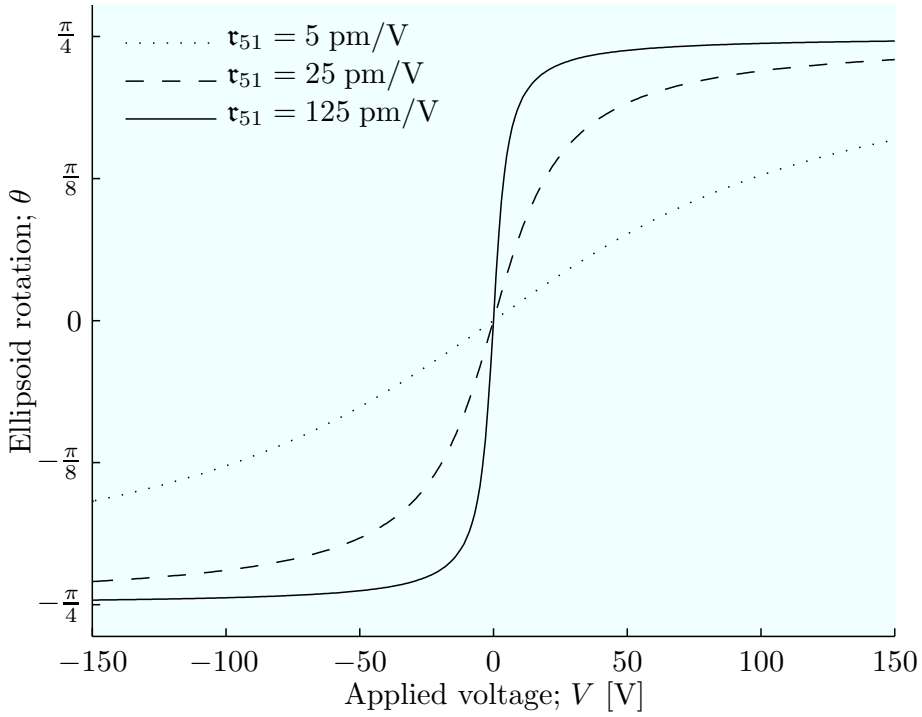


Figure 2.3: Rotation of index ellipsoid around $y$-axis as a function of modulation voltage. Calculated for $\Gamma = 0.8$, $n_o = 2.45$, $n_e = 2.45125$ and $d = 8$ µm.

Since a diagonal impermeability tensor can be written as $\eta_{ii} = \frac{1}{n_i^2}$, comparison with the diagonalised impermeability tensor in (2.10) gives the perturbed refractive indices as

$$n_1' = \left(\frac{1}{n_o^2} + \mathfrak{r}_{51}\frac{V}{d}\Gamma\tan\theta\right)^{-\frac{1}{2}} \tag{2.12}$$

$$n_2' = n_o \tag{2.13}$$

$$n_3' = \left(\frac{1}{n_e^2} - \mathfrak{r}_{51}\frac{V}{d}\Gamma\tan\theta\right)^{-\frac{1}{2}}. \tag{2.14}$$

For simplicity, it is customary to assume that $1/n_o^2 \ll \mathfrak{r}_{51}\Gamma V/d$ which allows the above expressions to be simplified using a first order Taylor approxima-

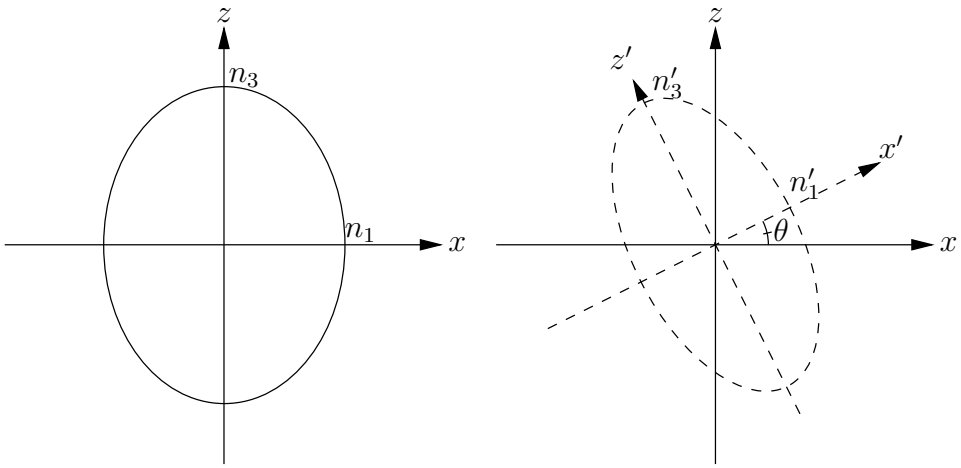


(a) Unperturbed polarisation ellipse. (b) Perturbed polarisation ellipse.

Figure 2.4: Unperturbed and perturbed polarisation ellipse.

tion. For completeness, this becomes

$$n_1' \approx n_o - \frac{1}{2} n_o^3 \mathfrak{r}_{51} \frac{V}{d} \Gamma \tan\theta \tag{2.15}$$

$$n_3' \approx n_e + \frac{1}{2} n_e^3 \mathfrak{r}_{51} \frac{V}{d} \Gamma \tan\theta. \tag{2.16}$$

However, due to the great computational power of modern computers, the exact expressions in (2.12) and (2.14) are used for all simulations in this project. The rotation of the index is illustrated in figure 2.4. The index ellipse describes the effective refractive index for a wave that is not polarised along one of the axes. Decomposition of a polarisation state onto the axes of the polarisation ellipse describes the birefringence of the propagating wave.

From (2.11) it is also possible to see that the sign of $\tan\theta$ is the same as that for $V$. With this in mind, (2.15) and (2.16) show that the perturbed refractive index is invariant to the sign of $V$.

The above theory is only exact for plane waves which propagates in an infinitely large piece of material. Optical waves confined by a waveguide will not propagate in modes with the bulk refractive index $n_i$ but rather with a reduced, effective refractive index. This index is denoted $n_{\mathit{eff},TEm}$ or $n_{\mathit{eff},TMm}$, where $m \in \mathbb{N}$ is the mode order. For small perturbations of the refractive index it is reasonable to expect that the effective refractive index is approximately linear with the perturbed refractive index. This can be expressed

as

$$n_{eff,TEm} \approx C_{TEm} n_1 - C^0_{TEm} \tag{2.17}$$

$$n_{eff,TMm} \approx C_{TMm} n_3 - C^0_{TMm}, \tag{2.18}$$

where $C_{TEm}$, $C_{TMm}$, $C^0_{TEm}$ and $C^0_{TEm}$ are constants. Simulations of ridge-type waveguides using FIMMWAVE supports the approximation. The constants in (2.17) and (2.18) were determined using FIMMWAVE with the assumption that the PLZT thin film is approximately isotropic with $n = 2.45$ and that the electrodes have neglible effect on $n_{eff}$. In these simulations the refractive index was changed for the entire PLZT thin-film. With an applied electric field however, the perturbation of the refractive index is dependent on the local electric field. This is also believed to have negligble effect as the electric field is approximately constant between the electrodes, a region which the optical modes are well confied to. Table 1 presents the simulated values of $C$ and $C_0$ for the fundamental $TE_0$ and $TM_0$ modes for selected ridge geometries. The table shows that $C_0$ is approximately constant with $C_0 \approx 0.17$ for both the TE and TM mode. However, the coefficient $C_{TE0}$ is clearly larger than $C_{TM0}$ for $h = 50$ nm while they are approximately equal for $h = 150$ nm. For this project $C_{TE0} \approx C_{TM0} \approx 0.92$ has been adopted for $h \approx 150$ nm; for $h \approx 50$ nm, $C_{TE0} \approx 0.98$ and $C_{TM0} \approx 0.92$ has been adopted.

Table 1: Approximate coefficients describing the linear relationship in (2.17) and (2.18) between the effective refractive indices of the fundamental $TE_0$ and $TM_0$ modes. Obtained through numerical simulations using FIMMWAVE.

| | $h = 50$ nm | | | | $h = 150$ nm | | | |
|---|---|---|---|---|---|---|---|---|
| | $C_{TE0}$ | $C^0_{TE0}$ | $C_{TM0}$ | $C^0_{TM0}$ | $C_{TE0}$ | $C^0_{TE0}$ | $C_{TM0}$ | $C^0_{TM0}$ |
| $W = 3.0$ µm | 0.98 | 0.17 | 0.93 | 0.20 | 0.92 | 0.17 | 0.92 | 0.17 |
| $W = 3.5$ µm | 0.98 | 0.17 | 0.92 | 0.17 | 0.92 | 0.16 | 0.92 | 0.17 |
| $W = 4.0$ µm | 0.98 | 0.16 | 0.92 | 0.15 | 0.92 | 0.15 | 0.92 | 0.16 |
| $W = 4.5$ µm | 0.98 | 0.15 | 0.92 | 0.15 | 0.92 | 0.15 | 0.92 | 0.15 |

Strictly speaking, the approximation in (2.17) and (2.18) are only valid for the case of $V = 0$ (ie, no actual perturbation) since the $x'z'$-axes are not parallel to the $xz$-axes, but rotated an angle $\theta$ around the $y$-axis. No theory has been found which can account for this rotation. It is therefore naively assumed that the optical axes of the effective refractive index are rotated equally to that of the crystal's optical axes. In other words, light propagates through the ridge-type waveguides with an effective refractive index ellipse oriented along the $x'z'$-coordinate system. The axis length of the ellipse are approximated by

$$n'_{eff,1} \approx n_{eff,TEm} \approx C_{TEm} n'_1 + C_{0,TEm} \tag{2.19}$$

$$n'_{eff,3} \approx n_{eff,TMm} \approx C_{TMm} n'_3 + C_{0,TMm}. \tag{2.20}$$

However, it is not obvious that $C$ and $C_0$ are invariant to $\theta$. It is conceivable that the waveguide geometry either amplifies or constricts rotation of the effective index ellipse. Due to time constraints and limitations in the available numerical simulation software, this relationship has not been further explored.

An optical wave that is linearly polarised along the $x'$-axis and is propagating along the $y$-axis will undergo a phase shift $\phi_{x'}$ given by (2.21) [3]. Similarly, a wave that is linearly polarised along the $z'$-axis and propagating in the $y$ direction will undergo a phaseshift given by (2.22).

$$\phi_{x'} = n'_{1,eff}\frac{2\pi}{\lambda_0}L \tag{2.21}$$

$$\phi_{z'} = n'_{3,eff}\frac{2\pi}{\lambda_0}L \tag{2.22}$$

Any wave propagating in the $y$-direction may be decomposed into two such orthogonal waves, one polarised along the $x'$-axis and the other along the $z'$-axis. The wave will experience a phase retardation $\Gamma_r$ between the two axes, which is given by

$$\Gamma_r = \phi_{x'} - \phi_{z'} = \frac{2\pi}{\lambda_0}L(n'_{1,eff} - n'_{3,eff}) \tag{2.23}$$

$$= \frac{2\pi}{\lambda_0}L\left(C_{TEm}n'_1 - C^0_{TEm} - C_{TMm}n'_3 + C^0_{TMm}\right) \tag{2.24}$$

$$\approx \frac{2\pi}{\lambda_0}L\left(C_{TEm}n'_1 - C_{TMm}n'_3\right), \tag{2.25}$$

where the last approximation is based on the previously established assumption that $C^0_{TEm} \approx C^0_{TMm}$. If there is a significant difference in $C_{TEm}$ and $C_{TMm}$ then this difference will effectively increase the birefringence between the two polarisations and increase $\Gamma_r$. According to table 1, this should be expected for $h = 50$ nm.

### 2.3.1 Phase modulator

A straight waveguide section with co-planar electrodes as shown in figure 2.5 will modulate the phase of a propagating wave according to (2.21) and (2.22) and is called a phase modulator (PM). As (2.23) shows, the birefringence between light polarised along the $x'$-axis and light polarised along the $z'$-axis induces a phase retardation $\Gamma_r$ between the two polarisations.

Jones matrix formalism can be applied to model a PM. A beam of light with an arbitrary input polarisation described by the Jones vector $\boldsymbol{J}_{in}$ in the $x, y, z$-coordinate system will exit the PM with a polarisation state (in

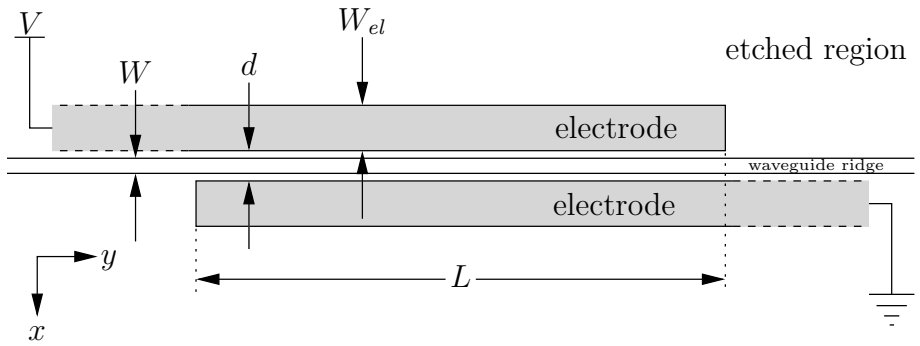


(a) Top view

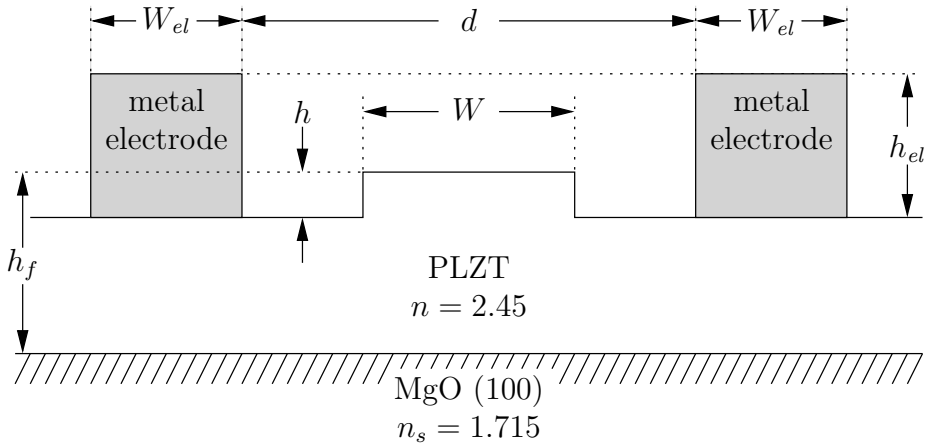


(b) Cross section

Figure 2.5: Ridge-type phase modulator geometry.

the $xyz$-coordinate system) given by

$$\boldsymbol{J}_{out} = R(-\theta)T_R R(\theta)\boldsymbol{J}_{in}, \tag{2.26}$$

where $T_R$ is a wave retarder matrix, $R(\theta)$ is a coordinate rotation matrix and $\theta$ is the rotation angle between the coordinate systems. $T_R$ is given by

$$T_R = \begin{bmatrix} \mathrm{e}^{j\Gamma_r/2} & 0 \\ 0 & \mathrm{e}^{-j\Gamma_r/2} \end{bmatrix}, \tag{2.27}$$

where $\Gamma_r$ is the phase retardation between the $x'$- and $z'$-axes defined in (2.25). $R(\theta)$ rotates $T_R$ an angle $\theta$ and is given by

$$R(\theta) = \begin{bmatrix} \cos\theta & \sin\theta \\ -\sin\theta & \cos\theta \end{bmatrix}. \tag{2.28}$$

When $\theta$ is given by (2.11) then $T_R$ is rotated from the $x'yz'$-coordinate system and into the $xyz$-coordinate system.

Since both $\Gamma_r$ and $\theta$ depend on the modulation voltage $V$, it is obvious that, in general, $J_{out}$ must also depend on $V$ as long as $J_{in}$ is constant. With an ordinary phase modulator which does not exhibit any rotation of the index ellipse, it is common to excite the modulator waveguide using light which is linearly polarised at a 45° angle to the optical axis. The polarisation state of the propagating wave will then be transformed depending on the phase retardation in the waveguide [3]. By placing a linear polariser at the output of the modulator, the transmitted intensity will dependend on the polarisation state of the light propagating in the waveguide.

In the case of a phase modulator with co-planar electrodes created in $c$-oriented PLZT where the polariser at the output is rotated an angle $\Theta$ to the $z$-axis, the output state can be described as

$$\boldsymbol{J}_{out} = R(-\Theta)T_{LP}(\Theta)R(-\theta)T_R R(\theta)\boldsymbol{J}_{in}. \tag{2.29}$$

In this expression, $T_{LP}$ is the a linear polariser oriented along the $x$-axis, given by

$$T_{LP} = \begin{bmatrix} 1 & 0 \\ 0 & 0 \end{bmatrix}. \tag{2.30}$$

The output intensity is given given by

$$I_{out} = \boldsymbol{J}_{out}^T \boldsymbol{J}_{out}^*. \tag{2.31}$$

Due to the complicated dependence of $\theta$ and $\Gamma_r$ on the modulation voltage $V$, it is difficult to intuitively grasp the behaviour of the system without losing many of the finer details. It is however relatively simple to model on

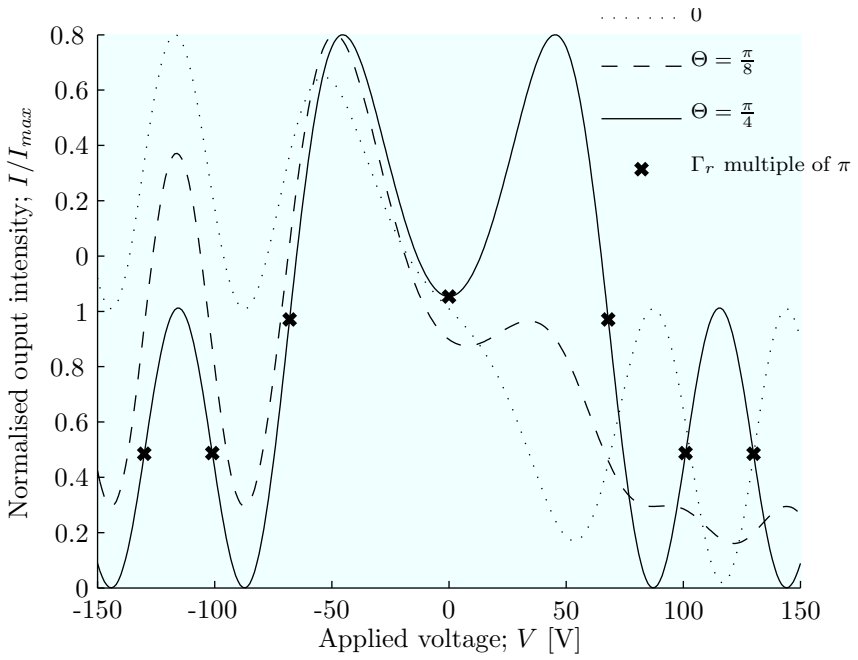


Figure 2.6: Simulated, normalised output intensity as a function of applied voltage for phase modulator excited with linearly polarised light 45° on the $z$-axis and with a linear polariser at the output. The ouput polariser is oriented $\Theta$ degrees on the $z$-axis. The markings on the curve for $\Theta = \pi/4$ indicate where $\Gamma$ is a multiple of $\pi/4$.

a computer. For modelling, it is natural to choose a linearly polarised input with equal components along the $x$- and $z$-axis. Thus the input Jones vector becomes

$$\boldsymbol{J}_{in} = \frac{1}{\sqrt{2}} \begin{bmatrix} 1 \\ 1 \end{bmatrix}. \tag{2.32}$$

Figure 2.6 was generated on the basis of (2.29) and shows a plot of the normalised output intensity $I_{out}/I_{out,max}$ as a function of the voltage $V$ for various values of $\Theta$. (The exact waveguide parameters are not given, as the plot's only function is to indicate the shape of the function.) This plot shows how the rotation of the index ellipse in general leads to an antisymmetric response. As previously discussed, the refractive index is perturbed equally for negative and positive voltages meaning that the only possible source of this assymetry is the rotation of the index ellipsoid, the direction of which depends on the sign of $V$. This is is due to the fact that decomposition of the polarisation vector onto the index ellipse depends on the sign of the rotation angle $\theta$. However, as shown by the figure, it is possible to counteract this assymbetry by crossing the ouput polariser with the input polarisation (ie, $\Theta = 45°$.)

In "regular" electro-optic materials (ie, no rotation of coordinate system)

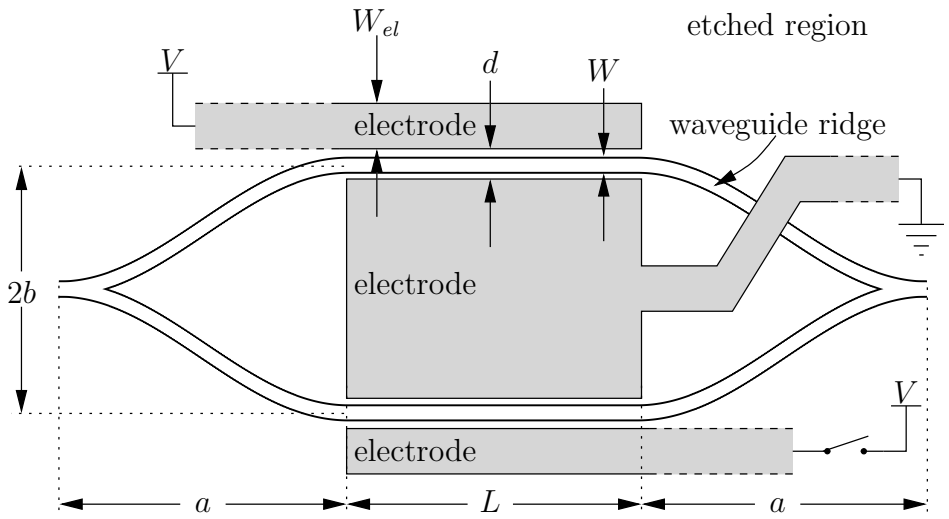


Figure 2.7: Top view of ridge type waveguide MZEOM. The indicated switch is external to the device.

where the minimas and maximas correspond to phase shifts that are multiples of $\pi$ [3]. This however is not the case for the modelled system due to the rotation of the index ellipse. This means that it is important to look at the voltage dependence of the system as a whole to evaluate its response and not just the voltage dependence of the phase retardation.

### 2.3.2 Mach-Zehnder modulator

Figure 2.7 shows the top view layout of the ridge-type waveguide MZEOM used for this project. In the figure, $a$ and $b$ are geometrical constants which primarily affects the losses in the y-splitter and y-combiner. $L$, $W_{el}$, $d$ and $W$ are the same as for the PM.

From the figure, it is obvious that a Mach-Zehnder electro-optic modulator (MZEOM) can be considered to be two phase modulators where the phase retardation $\Gamma_{r1}$ and $\Gamma_{r2}$ in each arm will in general be different. Linearly polarised light at the input of each arm can be described by

$$\boldsymbol{J}_{in,1} = \begin{bmatrix} A_x \\ A_y \end{bmatrix} \tag{2.33}$$

$$\boldsymbol{J}_{in,2} = K\mathrm{e}^{j\phi} \begin{bmatrix} A_x \\ A_y \end{bmatrix}, \tag{2.34}$$

where $K$ is a coupling coefficient allowing different amplitudes in each arm and $\phi$ is an inherent phase difference. Assuming that the material can be

regarded as linear for optical fields, then the combined output Jones vector becomes

$$\boldsymbol{J}_{out} = \boldsymbol{J}_{out,1} + \boldsymbol{J}_{out,2}. \tag{2.35}$$

Inserting the expression for $\boldsymbol{J}_{out}$ from (2.26) into $\boldsymbol{J}_{out,1}$ and $\boldsymbol{J}_{out,2}$ yields

$$\boldsymbol{J}_{out} = R(-\theta_1)T(\Gamma_{r1})R(\theta_1)\boldsymbol{J}_{in,1} + R(-\theta_2)T(\Gamma_{r2})R(\theta_2)\boldsymbol{J}_{in,1}. \tag{2.36}$$

As in the case of a phase modulator, the ouput intensity is $I_{out} = \boldsymbol{J}_{out}^T \boldsymbol{J}_{out}^*$.

It is clear that both $\Gamma_{r1}$ and $\Gamma_{r2}$ can be modulated by applying a voltage across the corresponding modulator arm. As indicated in figure 2.7 it is assumed that the voltage applied over arm number 2 is either undefined (and assumed to be 0 V) or equal to the voltage $V$ across arm number 1. Since the grounded electrode is placed between the two arms, the voltages in arm number 1 and arm number 2 will effectively carry the opposite sign. Figure 2.8 shows the simulated response of the system based on (2.36). The selected parameters are arbitrary, but the figure illustrates well how the system behaves in general. The figure clearly shows that by applying a the same voltage to both arms, the voltage required to go from an intensity peak to a neighbouring valley approximately halves. Since the effective phase retardation is doubled, this is as expected. However, it is clear that by modulating both arms there is a clear reduction in modulation depth (ie, the difference in normalised intensity between a intensity peak and valley) close to $V = 0$ V. This is explained by the rotation of the coordinate system. The electric field in the two arms are directed in opposite directions, rotating the coordinate system in opposite directions. Maximum modulation depth will be achieved when the two coordinate systems are parallel, which happens when $\theta_1 = -\theta_2 = \pi/4$, or equivalently $V \to \infty$.

Further simulations show that the modulation depth can be increased by reducing the birefringence $\Delta n$. As shown for the phase modulators, a reduction in birefringence does also decrease the voltage required to go from an intensity peak to an intensity valley.

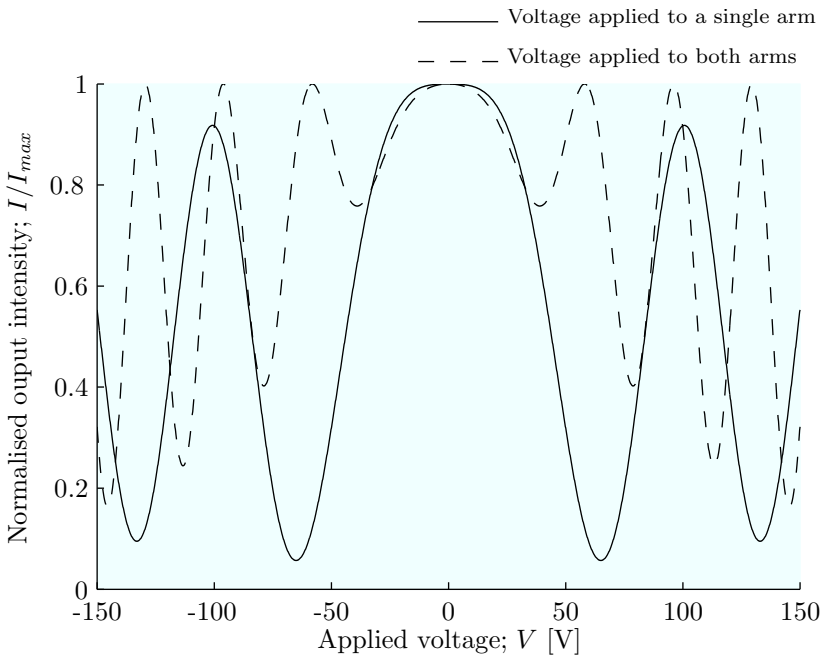


Figure 2.8: Simulated, normalised output intensity as a function of applied voltage for an arbitrary Mach-Zehnder electro-optic modulator excited with linearly polarised light.

# 3 Fabrication

The devices were fabricated in the local clean room laboratory using photolitography, wet etching and electron beam physical vapour deposition (EBPVD) for lift-off metallisation. To achieve good coupling of light into the waveguides, the end faces were cut and polished. The devices were fabricated in epitaxial, *c*-oriented PLZT thin films on polished, MgO (001) substrates. The substrates are delivered as 10 mm × 10 mm × 0.5 mm dies and commercially available [6]. Onto these, 500 nm thick thin-films were grown by sputter-deposition at the department [2]. The thin films are used "as grown" without any post processing before fabrication. The majority of the procedures described in this chapter have been established by previous work at the department and have only been slightly modified for this project.

## 3.1 Clean room procedure

The primary steps in the fabrication of the devices were performed in the clean room facility at the department. A detailed list of the equipment that was used is given in appendix C. The process involves two photolitography steps using a contact aligner, wet etching of the PLZT thin film and lift-off metallisation using EBPVD. Figure 3.1 gives a brief overview of the general process employed. The steps needed to perform this process are presented in the following sections.

### 3.1.1 Cleaning

If the die surface is contaminated then it is necessary to clean it before fabrication can start. Failing to properly clean the sample will inevitably result in defects. Cleaning is not always necessary if the sample has come directly from the film growth process without having been exposed to the environment or other processes. The following cleaning procedure is also used to strip resist from the sample.

In order to clean the sample, it is sprayed with acetone and then submerged in acetone. Acetone is a solvent and this treatment will remove common stains and particles. As complementary solvents, isopropanol (IPA), ethanol or both are used to rinse off any residue left after the acetone treatment. After rinsing, the sample is dried using compressed nitrogen.

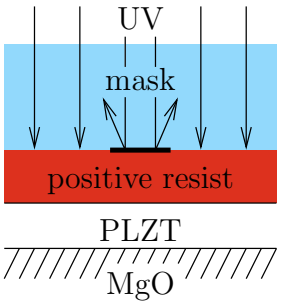


(a) A clean sample is coated with positive resist and UV light is shone onto it through a chromed-glass mask.

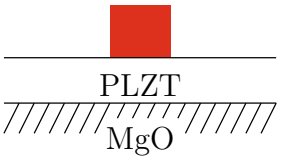


(b) The sample is then developed, removing the exposed photoresist.

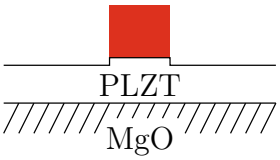


(c) During etching, the photoresist protects the area underneath it, creating the waveguide structure.


(d) Cleaning off the positive resist reveals the waveguide structure.

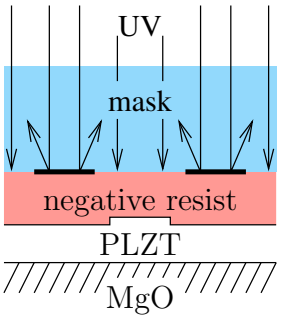


(e) The sample is coated with a negative resist and UV light is shone onto it through a chromed-glass mask.

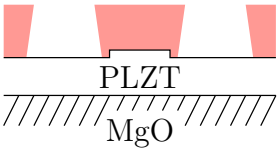


(f) The sample is developed, removing the unexposed photoresist. To facilitate lift-off, undercut (i.e. negative slope) sidewalls are desired.

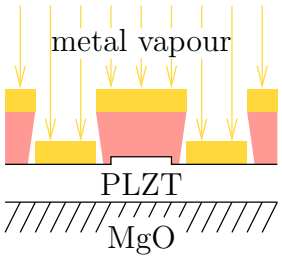


(g) Metal is deposited onto the sample using EBPVD.

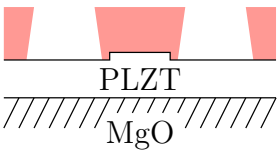


(h) Cleaning off the negative resist reveals the finished structure.

Figure 3.1: Summary of fabrication process.

### 3.1.2 Priming

Before spinning on resist it is necessary to clean the sample according to the procedure in the previous section. It is also important to minimise the amount of moisture on the sample as moisture prevents good adhesion between the film and resist. To achieve this, a dehydration bake on a 100 °C hot plate is performed for 6 min, evaporating moisture adsorbed on the film surface. The sample is then placed on the vacuum chuck of a spinner. One or two drops of hexamethyldisilazane (HMDS) is dripped onto the sample while it is stationary. The sample is then spun for approximately 20 s at 4000 r/min, spinning off excess HMDS and distributing the remaining HMDS evenly across the sample. After the HMDS has been applied, the sample is left to rest for 60 s. HMDS is a commonly used chemical primer that improves adhesion between the thin film and the resist.

### 3.1.3 Spin coat

For the etching, a positive photo resist is used to protect selected parts of the die from being exposed to the etchant. Similarly, a negative photo resist is used to protect selected parts of the die from getting metallised. In order to perform these tasks it is important to coat the die with a uniform layer of the relevant photo resist.

With the sample still on the vacuum chuck of the spinner, four or five drops of photo resist are dripped onto the sample, covering it. The sample is then spun for 20 s at 4000 r/min, distributing the resist evenly across the sample. The thickness of the resist $h_r$ is primarily dependent on the viscosity of the resist and the spin speed. The viscosity varies between different brands of resist, but for the two used in this project, 4000 r/min was appropriate. Table 2 shows the expected thickness of both the positive and negative resists that were used.

Table 2: Properties of the resists that were used. Thickness listed for 20 s @ 4000 r/min

| Type | Name | $h_r$ | Exposure time |
|---|---|---|---|
| Positive | Microprosit S1818-G2 | 2 µm | 6.2 s |
| Negative | micro resist ma-N 1420 | 1.75 µm | 22 s |

After coating the sample with resist it is important to inspect the coating, making sure that it has a uniform thickness. A uniform coating will have a uniform colour when viewed at an angle while there will be a colour gradient if the thickness is not uniform; the latter being caused by interference. Such a variation in film thickness is usually not acceptable except at the edges where, due to surface tension, there will be a build-up of resist. If a colour

gradient is observed other places then the sample should be stripped off according to section 3.1.1 and the priming and spin coat steps redone.

After achieving a uniform resist thickness the sample is put through a soft-bake process. The purpose of the soft bake is to alter the properties of the resist in such a way that it is ready for exposure. By baking the sample, most of the solvents in the resist are driven off. The softbake improves the adhesion to the film, improves the uniformity and solidifies it. For both of the resists used in this project, the soft-bake is performed on a hot-plate with a temperature of 100 °C for 60 s.

### 3.1.4 Alignment and exposure

After the soft-bake, mask alignment and exposure is performed with a contact aligner. For the devices in this project, two different masks were used; the first mask is a positive mask (ie, meant for positive resist) with the pattern for waveguides and the second mask is a negative mask with the pattern for electrodes. Both the masks used are chrome covered glass plates. The part of the pattern on the masks that were used is the size of one die and contains various waveguides including Mach-Zehnder interferometers and straight waveguides. Both modulator types have complementary electrode patterns on the electrode mask. The mask layout will be further detailed in section 4.

In order to transfer these two patterns onto a die, the die is first coated with photoresist as described in the previous sections. Positive resist is used for the waveguide mask and negative resist for the electrode mask. The die is then placed onto the vacuum chuck of the contact aligner and the relevant mask is cleaned and mounted into the system with the chrome layer down, towards the die. To facilitate independent movement of the mask and die, there is a small gap between these at this point. Using the mask aligner controls and the microscope, the mask is aligned with the die. For the first exposure (figure 3.1a,) the die has a featureless surface and the waveguide mask is simply centered on the die and aligned with the desired angle to the sides of the die. For the second exposure (figure 3.1e,) the waveguides have been etched into the thin film. Thus, the electrode mask must be carefully aligned with the existing waveguide structure.

After alignment, the mask and die are brought into contact with each other. The UV light is then engaged, exposing the photoresist. The duration of the exposure depends on the resist. The exposure times in table 2 were found to be suitable in order to achieve the desired linewidths. However, some variation in linewidth was found, which is believed to be attributed primarily to variation in the intensity of the UV light source.

### 3.1.5 Development

After exposing the photoresist it is ready to be developed. In the case of positive photoresist, the parts of the photoresist that has been exposed to UV light have been softened and are soluble in the developer chemical. The negative photoresist behaves in an opposite manner with the exposed parts hardening and becoming insoluble in the developer.

In order to develop the photoresist, the die is submerged in developer with gentle agitation. After a set amount of time, the die is removed from the developer and promptly dipped in de-ionised (DI) water for $\sim 20$ s in order to stop the development and clean off the developer. The die is then spun dry. Two different developers were used for this project; one for the positive photoresist and one for the negative. Table 3 lists these developers and the development time that was used. For the negative resist a relatively long development time was used in order to achieve undercutting. Undercutting means that the sidewalls slopes inwards as shown in figure 3.1f. This is done in order to facilitate effective lift-off.

Table 3: List of developers.

| Type | Name | Development time |
|---|---|---|
| Positive | Micro Resist ma-D 533 | 45 s |
| Negative | Shipley Microposit MF-86 | 85 s |

After developing the resist it is important to inspect the result using microscopy. If there are significant defects or significant deviation in the line width from the mask line width, then the resist needs to be stripped off following the procedure in section 3.1.1 and the die re-coated, re-exposed and re-developed. However, if this process is repeated too many times stains and defects tend to accumulate, making it more difficult to create a defect-free pattern. Particularly, the positive photoresist has been observed to slightly etch on the PLZT thin film, degrading the surface somewhat. Thus, small defects should be tolerated when possible.

If the next step is etching (ie, positive resist and the waveguide mask was used,) then the resist needs further curing to be able to withstand the etchant better. This is achieved by performing a hard-bake on a hot plate with a temperature of 130 °C for 120 s.

### 3.1.6 Etching

After developing and hard-baking the positive resist, the remaining photoresist pattern will protect the PLZT under it. For this project a wet etch

Table 4: Etchants used for etching waveguides.

| | | |
|---|---|---|
| PZT etchant | $NH_4Cl$ | 10.7 g |
| | $H_2O$ | 76 ml |
| | B-HF | 10 ml |
| | HCl | 20 ml |
| PLZT etchant | PZT etchant | 1 unit |
| | $H_2O$ | 1 unit |
| Diluted nitric acid | 65% $HNO_3$ | 1 unit |
| | $H_2O$ | 1 unit |

procedure is used due to simplicity. Due to the similarity between PLZT and $Pb(Zr,Ti)O_3$ (PZT), the wet etching procedure is based on the procedure presented in [7]. The components of the etchant are listed in table 4. A batch of PZT etchant was available for the project and the PLZT etchant was mixed on a per-session-basis, causing variation in etch rate.

According to [7], the etching process leaves a PbClF residue. To remove this residue, the die is submerged in diluted nitric acid with the consentration in table 4.

Etching is perfomed by submerging the sample in the PLZT etchant for a few seconds. The exact length of time depends on the desired etch depth. The die is then immediately submerged in DI water for 30 s, diluting the etchant and stopping the etching process. Then it is submerged in the diluted nitric acid for 30 s, cleaning off the residue from the etching process. Finally, to stop any reaction with the nitric acid and clean the die, it is submerged in DI water for 30 s before being blown dry with compressed nitrogen. Figure 3.1c shows the expected structure at this point. Cleaning it using the procedure in section 3.1.1 gives the result illustrated in figure 3.1d.

The number of seconds the die is submerged in the PLZT etchant determines the etch depth. For the etchant used in this project, the etch rate was found to be approximately 10 nm/s. However, since the etching time is controlled manually and the PLZT etchant is mixed for each session, the actual etch rate varies. The actual etch depth is therefore measured using the laboratory's mechanical step index profiler (after removing the positive resist.)

For this project devices with $h \approx 50$ nm and $h \approx 150$ nm were produced.

### 3.1.7 Metallisation

After etching a die, the die is coated with negative resist, exposed and developed (sans hard-bake.) The die is then mounted for EBPVD on a sample holder. Later in the process, the end surfaces will be polished to facilitate

coupling of light into the waveguides. Polishing on a die with a metal layer may cause bits of metal to break loose which in turn may disturb the polishing process and induce micro scratches. To avoid this problem, the edges of the die is masked out with household aluminium foil, only leaving the essential parts of the metal structure (ie, electrodes and contact pads.)

The sample is then inserted into the vacuum chamber of the EBPVD-system and the metal deposited. First a 10 nm layer of platinum is deposited and then a 200 nm layer of gold. The platinum layer is used to improve adhesion between the metal and PLZT. No significant problems were experienced in this process as long as the electron-beam current was not driven too high, causing sputtering.

### 3.1.8 Lift-off

After the metal has been deposited the die is removed from the EBPVD-system. Except for the edges which were masked out by aluminium foil, the entire die is covered by metal. By removing the underlying negative photoresist, only the electrodes and contact pads will remain as these have been deposited directly onto the PLZT thin film and not onto the photoresist. In order to remove the negative photoresist the die is first soaked in acetone for 15 min. Subsequently, it is sprayed with acetone from an airbrush, removing most of the resist. In order to remove the resist in narrow spaces (such as in the gap between electrodes) the die is placed in an acetone filled beaker. This beaker is then covered and placed into an ultrasonic bath for 5 min. In some cases it is necessary to increase the time in the ultrasonic bath. Should any resist remain after this treatment it is necessary to remove it using an acetone soaked brush or swab. However, this should be done carefully in order to avoid scratching the surface and waveguides excessively. After all of the resist and excess metal has been removed, the sample is cleaned and inspected for defects. Figure 3.1h illustrates the end result of the process.

## 3.2 Cutting

After the die has been processed in the clean room the end surfaces need to be cut. As mentioned in section 3.1.3, there is a buildup of resist at the edges. The excess photoresist thickness at these places is so large that the exposure and development process do not expose the underlying PLZT thin film in these areas. As a consequence, the waveguides do not extend all the way to the edges. The edges that are perpendicular to the waveguides are cut, in order for the waveguides to extend all the way to the edge. The cuts are performed using a rotating diamond saw at 100 r/min with a pressure

of approximately 50 g. After the cut there should still be a few millimeter from the edge to the metal electrodes, giving room for polishing.

### 3.2.1 Polish

The recently cut end surfaces have high surface roughness which leads to large amounts of incident light being scattered at the end surface. As a result, it is not possible to efficiently couple light into the waveguides. To achieve efficient coupling, it is necessary to polish the end surfaces. This is performed using a polishing machine based on rotating lapping films.

Before the sample can be polished it is mounted on a sample holder compatible with the polishing system. First, the sample holder is put on a hot plate heated to 200 °C. With the sample holder on the hot plate, a thin layer of hot mounting wax is applied. A thin glass plate is then put on top of the wax layer and another thin wax layer is applied on top of the glass. Then the die is mounted with the waveguide side towards the glass. A few millimeters of the die is left hanging off the edge of the sample holder in order to facilitate polishing. In addition, the die should go slightly farther out than the glass plate. If the glass plate extends the farthest out, there is a risk of it breaking and damaging the edges. The purpose of the glass plate is to support the die, preventing the edges from chipping.

After the die has been mounted properly on the sample holder it is taken off the hot plate and left to cool for a few minutes, solidifying the mounting wax. The sample holder is then mounted in the polishing machine and aligned with the polishing surface so that the sample is polished approximately perpendicular to the waveguides. Polishing is then performed with diamond lapping films. The film is set to rotate at 30 r/min while the sample is set to oscillate across it. The rotation should be directed away from the waveguide side of the die and the edge of the die should be perpendicular to the direction of rotation. A continuous stream of water should be applied when polishing with films with a grain size larger or equal to 3 µm. When polishing with films with smaller grain size a lubricant is used instead. The purpose of the water and lubricant is to quickly remove debris, cool the sample and lubricate the process.

For this project, diamond lapping films with grain sizes of 30 µm, 15 µm, 6 µm, 3 µm, 1 µm and 0.5 µm were used, in that order. Between 0.5 mm and 1.5 mm should be polished off when polishing with the 30 µm film. For the subsequent films, a rule of thumb is to polish off approximately three times the previous grain size (eg, polish off 18 µm with the 3 µm film.) However, from experience, a couple of minutes with each film should suffice. After each polishing, the end surface should be inspected. If it does not have an uniform

look, then further polishing is needed with that grain size. A good end result is characterised by a straight interface between the die and the wax and a transparent end surface without any scratches being visible through a 40× microscope.

When one side has been completed, the sample holder with the die should be put back on the 200 °C hot plate. After a few minutes, when the die can be easily pushed around on the sample holder without resistance, the sample can be turned around and the polishing procedure repeated. Applying force when turning the die will inevitabely result in serious scratches on the die surface.

After finishing the polishing procedure on both sides it is important to remove the mounting wax. This is done by first heating the sample holder and die on the 200 °C hot plate so that the die can be pushed around on the sample holder without resistance. Then the die is removed and immediately submerged in acetone and left there for a few minutes while applying gentle agitation. To avoid acetone and wax residues the sample is then resubmerged in fresh acetone for some additional minutes. After the acetone treatment it is immediately submerged in ethanol for a few minutes before it is dried off by placing the die onto a hot plate heated to 100 °C. Using a microscope, the die is then inspected for any residual mounting wax. If any is found, then the cleaning process needs to be repeated. Difficult wax stains may be removed by using a swab and some acetone. However, this method carries significant risk of scratching the surface and chipping the edges.

After successfully polishing the die the end result is a functional device ready for testing.

## 3.3 Critical stages and yield

Although the applied process has been developed primarily for small scale experimental purposes, the process yield should be mentioned with suggestions on process improvements. Experience shows that most problems come after the first photolitography step.

Alignment of the second mask over the etched waveguide structure has been found to be difficult with the *MA56* contact aligner. Figure 3.2 illustrates how the waveguides can be offset from the ideal center position between the electrodes. The primary two factors that contribute to this problem are a shallow depth of focus and a lack of contrast. Both these problems stem from the optical microscope on the contact aligner. The shallow depth of focus makes it difficult to keep both the mask and the underlying waveguide in focus while aligning. This problem can be alleviated by using less magnification, but then it becomes hard to resolve the narrow gap between the

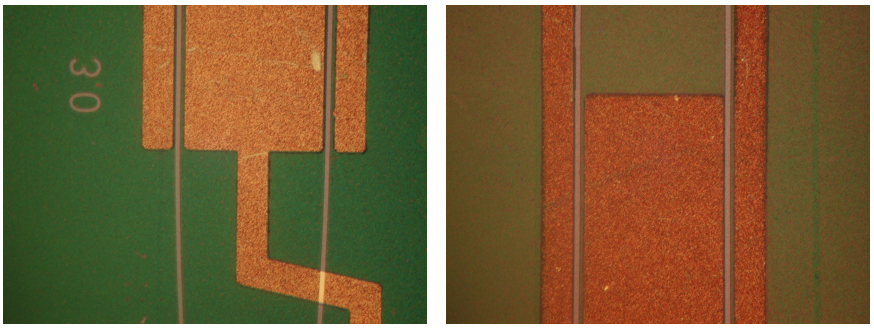


Figure 3.2: Example of misaligned electrodes at both end of an MZEOM with $W = 3$ µm

electrodes into which the waveguides should be aligned. The problem is also exacerbated for shallow waveguides (etch depths below 50 nm) due to low contrast. The photoresist layer on top of the waveguide structure does also decrease the contrast.

Single mode waveguides are desired in order to achieve results which are simple to analyse. Simulations of ridge type waveguides in FIMMWAVE show that with the available waveguide mask, single mode waveguides can be acheived with $h \lesssim 15$ nm. However, due to the reduced contrast at shallow etch depths, alignment would be problematic. As a consequence, all the waveguides that were fabricated for this project were multi mode.

The obvious solution to these problems is to use another aligner with better optical equipment. Another possible solution could be to incorporate suitable alignment marks on the masks. Decreasing the photoresist thickness would probably help too by increasing the contrast.

After clean room processing, the polishing presents several challenges. As mentioned previously, the die is mounted with the thin film side towards the sample holder using hot mounting wax. When mounting and unmounting the die, as well as when handling the die while mounted on the sample holder (eg to turn it around for polishing on the opposite side), there is a significant risk of scratching the surface. At least one die was completely ruined by excessive scratching. It is believed that this problem is exacerbated by the fact that the wax layer between the die and the glass plate was too thin. A thin wax layer would increase the probability of sites with direct, high friction contact between the die and the glass plate. Small particles would also penetrate the wax layer more easily when it is too thin.

The solution to this problem would be to simply increase the amount of wax used. However, it is believed that this increases chipping of the thin film edge due to reduced support. Balancing these two requiremets is difficult, especially since the process of depositing wax is not well controlled. How-

ever, an experienced operator should be able to approach some optimal wax thickness.

Another, more radical, solution would be to alter the waveguide design in order to make it more resilient to scratches. One possibility is to deposit a protective layer of some material on top of the thin film and electrodes. The protective layer would remove the possibility of chipping at the PLZT interface. One possible material is MgO which can be deposited using EBPVD. However, such a layer could affect the properties of the PLZT thin film by straining on the surface or otherwise damage it. It would also alter the optical properties of the waveguide, requireing a complete redesign. Holes would also have to be made in the protective layer over the electrodes to facilitate electrical contact. This would introduce another process step, either as an etching process or a lift-off process.

Another possible solution to problems during polishing would be to redesign the devices to use other ways of coupling light into the waveguides. For instance, it may be possible to use grating side couplers which are fabricated entirely by etching a grating into the thin film. A high quality coupler would allow light to be coupled into the waveguide without also coupling into the thin film. Polishing of the ouput surface would then be less critical as light will mainly propagate through the waveguide structure of the modulator and thus be modulated regardless of scattering at the output.

For the work performed as a part of this project, the fabrication process had a yield of approximately 50% for the finished devices. However, each device contained several modulators of which only a limited number was usable. Thus the total yield is lower than 50%.

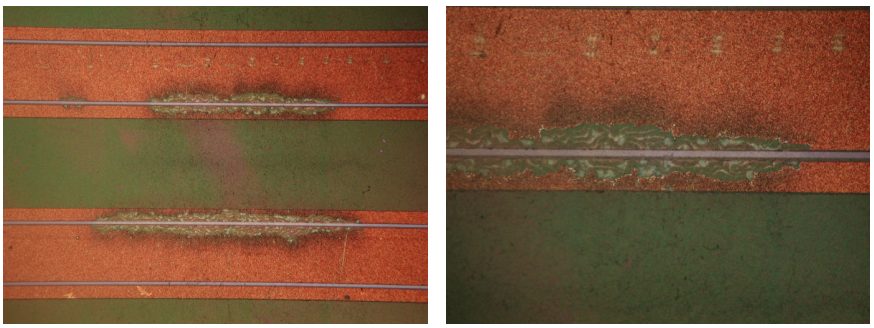

(a) 20× magnification (b) 50× magnification

Figure 3.3: Typical examples of damage caused by dust particles causing arching between high voltage electrodes.

Experience shows that when a large voltage (eg, $\sim 150$ V) is applied across the electrodes, localized damage to the electrodes and nearby waveguides

may occur. Figure 3.3 shows an example of this phenomenon. These defects correlate well with previously observed dust particles between the electrodes at the damage sites. The defects also only occured between electrodes that had been powered. It is reasonable to assume that when subjected to a high voltage the dust particles will cause explosive arching, damaging the surrounding area; wax residues can also cause this type of damage. This effect was responsible for destroying several waveguides and great care should be taken to avoid excessive dust.

# 4 Photolitography mask layout

Photolitography masks made from chrome on glass were used in the fabrication of the electro optic modulators. The chrome layer reflects incident light, preventing exposure of the underlying photoresist. As mentioned in the previous section, two masks are required. One for creating the waveguide pattern and one for creating the electrode pattern.

The geometrical parameters of the MZEOMs were presented in figure 2.7 and the geometrical parameters of the PMs in figure 2.5. The masks for eight MZEOMs and eight PMs with slightly different geometrical parameters are combined to form a single device. The MZEOMs are denoted MZ1 through MZ8, while the PMs are denoted PM1 through PM8. Table 5 lists the parameters of the mask for each of the modulators. Due to variations in processing $d$, $W$ and $W_{el}$ are considered to be nominal values only.

Table 5: Geometrical values of the masks used for producing the modulators.

(a) Geometrical values for Mach-Zehnder electro-optical modulators.

| Designation | $W$ [µm] | $a$ [µm] |
|---|---|---|
| MZ1 | 4.5 | ∼545 |
| MZ2 | 4.0 | |
| MZ3 | 3.5 | |
| MZ4 | 3.0 | |
| MZ5 | 4.5 | ∼630 |
| MZ6 | 4.0 | |
| MZ7 | 3.5 | |
| MZ8 | 3.0 | |

(b) Geometrical values for phase modulators.

| Designation | $W$ [µm] |
|---|---|
| PM1 | 4.5 |
| PM2 | 4.0 |
| PM3 | 3.5 |
| PM4 | 3.0 |
| PM5 | 4.5 |
| PM6 | 4.0 |
| PM7 | 3.5 |
| PM8 | 3.0 |

(c) Common geometrical values for mask.

| $b$ | $d$ | $l$ | $W_{el}$ |
|---|---|---|---|
| 50 µm | 8 µm | 3 mm | 20 µm |

The modulators are laid out in a pattern as indicated by the stylized drawing in figure 4.1. The drawing is not to scale and lacks other waveguide devices which were also present, but not used for this project. In the figure, the blue colour indicate the waveguide mask while the black colour (sans letters) indicate the electrode masks. The lines connecting the electrodes to the larger contact pads are 20 µm wide while the square contact pads are 250 µm × 250 µm large. The smaller contact pads are connected with 20 µm lines which are terminated in larger contact pads that are 250 µm wide and extend to the edge of the mask. The large electrodes at the top and bottom

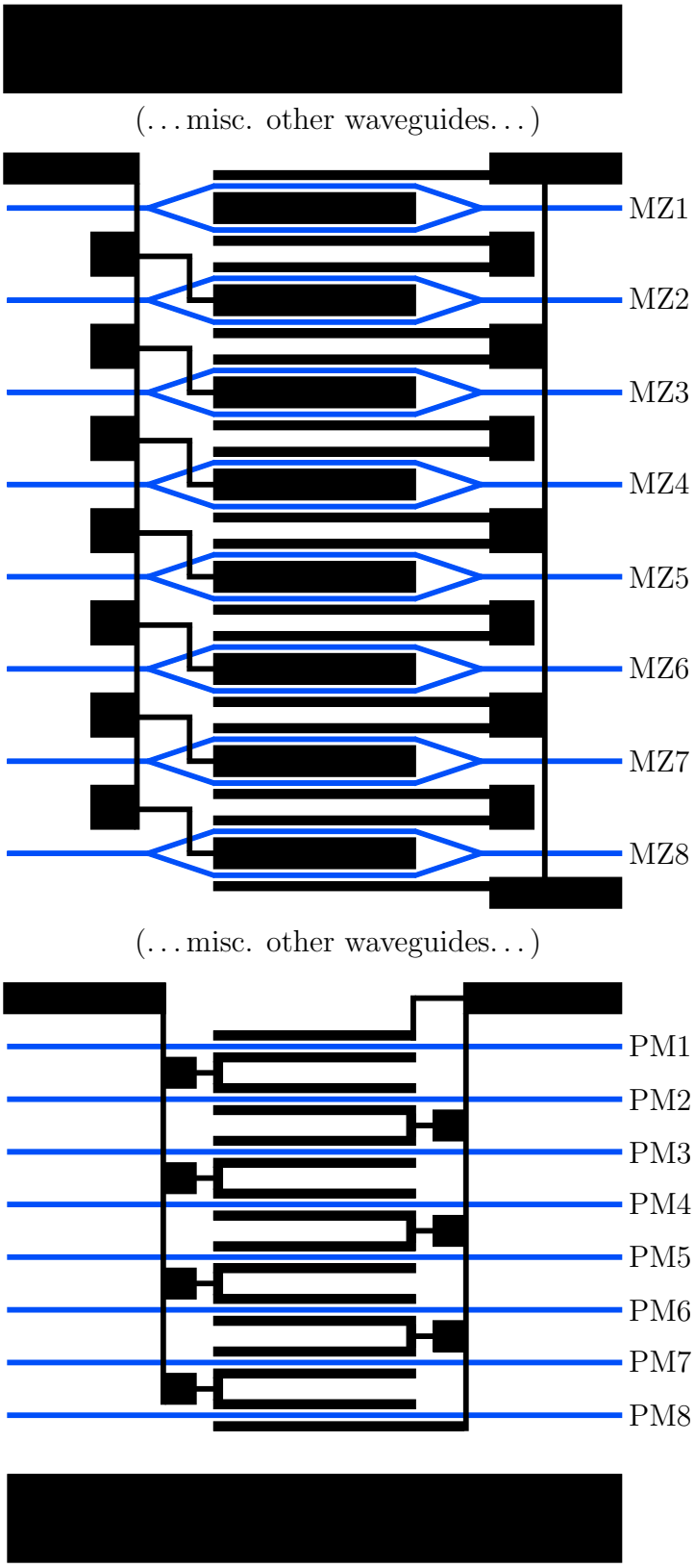




Figure 4.1: Stylized layout of the masks that were used. Blue colour indicates waveguide mask while black colour (sans letters) indicate electrode mask.

are provided to facilitate bonding the smaller pads to external contacts, but they were not used for this project.

# 5 Experimental setup

In order to measure the electro-optic effect, a setup which allows the output intensity $I$ to be measured as a function of applied voltage $V$ is needed. Figure 5.1 shows a schematic drawing of the setup that was employed for this project. A complete list of the equipment that was used is given in appendix C.

The primary components of the setup is the optical path (marked with arrows) and the ability to apply a voltage to the contact pads using probe needles. Light at the $\lambda = 1.55$ µm wavelength enters the optical path from a continuous wave laser driven by 100 mA and is first injected into a common fibre polarisation-controller (FPC). This controller works by stress induced birefrigens in a single mode fibre creating three wave plates; a quarter-wave plate followed by a half-wave plate followed by a quarter-wave plate allows the controller to create an arbitrary polarisation state on the output from any polarised light of any arbitrary state [3]. For the purpose of measuring the electro-optic effect, light that is linearly polarised either along the $x$- or $z$-axis or 45° on the $z$-axis is used.

The polarised light exiting the FPC is coupled into a fibre which ends in a taper. This fibre is ideally polarisation maintaining, but in a few cases the setup has been used with non polarisation maintaining tapered fibres; no problems can be attributed to this as long as the polarisation is controlled. The purpose of the tapered fibre is to focus the light onto the end face of a waveguide on the device under test (DUT). If there is little scattering and a good overlap between the waveguide mode and the light focused onto it then light will be coupled into the waveguide. A similar tapered fibre is mounted at the output of the waveguide allowing light to be coupled from the waveguide and into the fibre. The device and tapered fibres are mounted on a flexural stage which allows the input and output fibres to be translated along the $x$-, $y$- and $z$-axes using micrometers. The DUT is mounted between the tapered fibres and it can be rotated around the $z$-axis and tilted around the $y$-axis using micrometers. The DUT can also be translated along the $x$-axis and coarsely translated along the $z$-axis.

Depending on the experiment being performed the output fibre is connected either directly to a infrared detector or to a polarising beam-splitter (PBS). In the latter case, one of the PBS outputs is connected to the detector. The detector is connected to an oscilloscope through a generic amplifier and the voltage measured by the oscilloscope should be proportional to the total power at the detector.

In order to facilitate measurements of the electro-optic effect signal generator 1 is connected to a 100× voltage amplifier with the ability to produce voltages

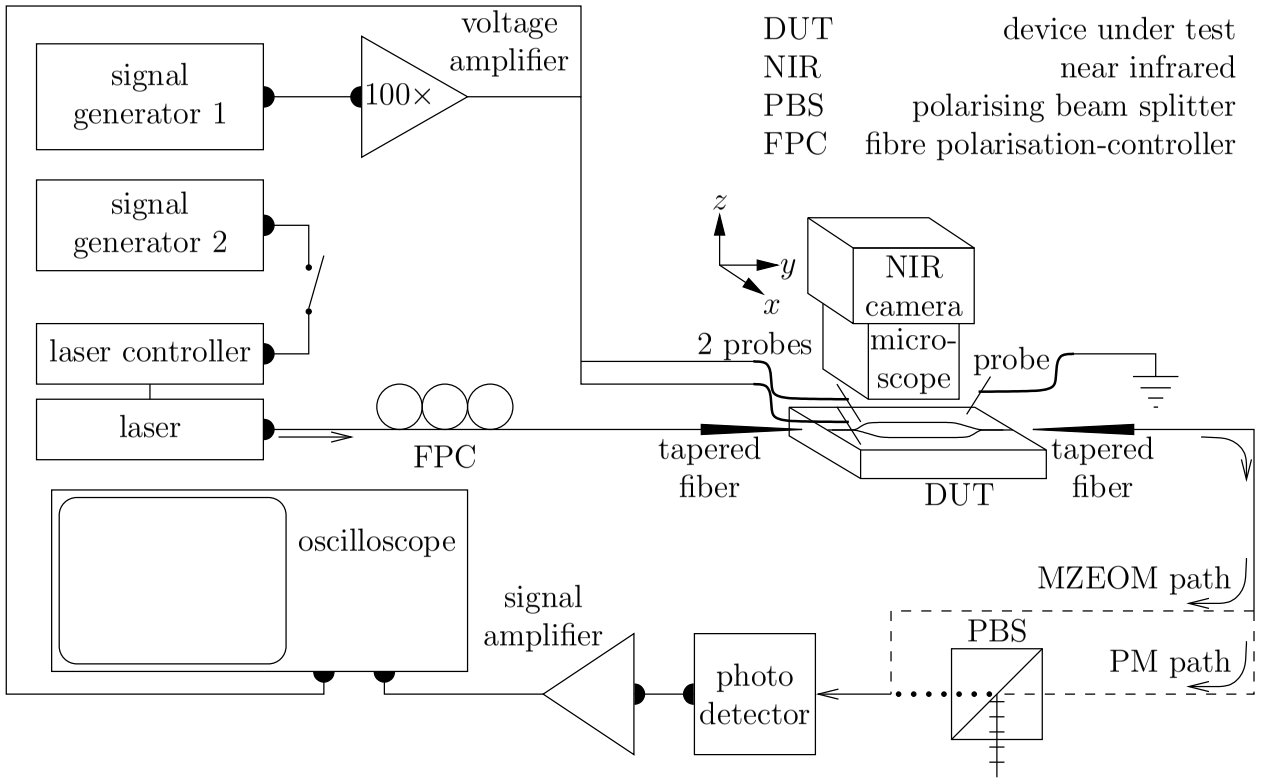


Figure 5.1: Schematic overview of the experimental setup. Light should be passed through the PBS if the DUT is a PM, but not if it is an MZEOM. The exact equipment that was used is listed in table 10.

as large as ±400 V. The output of this amplifier is connected to probe stations with micromanipulators. Using the micromanipulators, which can translate the probes along all the three major axes, it is possible to accurately place needles onto the contact pads on the device.

## 5.1 Fibre alignment

To ease alignment of the tapered fibres with the waveguides, a microscope with a near infrared (NIR) camera is utilised. The tapered fibres are first aligned with the waveguides in the $xy$-plane; separated by a few micrometres from the end face of the DUT. Light propagating through the thin film is scattered out of the surface making it possible to observe the path of the light in the thin film using the NIR camera. Thus, when the tapered fibre is properly aligned with the waveguide on the $y$-axis, the waveguide will light up clearly as shown in figure 5.2.

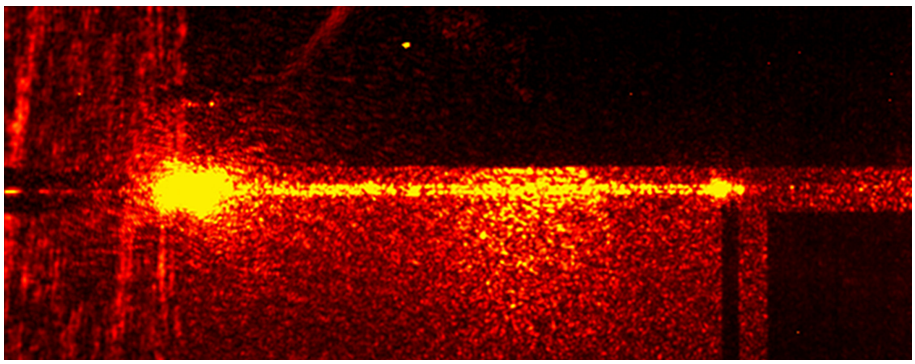

Figure 5.2: NIR image of properly aligned tapered fibre exciting guided modes in the waveguide. The tapered fibre is visible to the left. High, abrupt absorption observed to the right is due to metal crossing the waveguide.

The output fibre is primarily aligned along the $z$-axis manually while modulating the laser with a 1 kHz sine signal with an amplitude of 4 V from signal generator 2. When the fibre is successfully aligned the transmitted signal is detected by the infrared detector and a clear sine appears on the oscilloscope. After the initial alignment, minor adjustments on all axes are performed, maximising the transmitted 1 kHz signal. Experience shows that sufficient transmission of light can not be expected on all modulators due to local damage on the waveguides scattering most of the light or due to poor polishing preventing sufficient amounts of ligth to be coupled into the waveguides.

It is possible to perform the alignment procedure without a NIR camera, but the process is significantly more difficult. Experience shows that spurious

modes which are guided in the film or substrate and not in the waveguides will often complicate the alignment procedure.

## 5.2 Measurements

After the fibres have been aligned and light is efficiently transmitted through a modulator, a voltage is applied to the electrodes. Depending on the modulator used, either two or three probes are used. In the case of a PM the ground probe and one probe connected to the voltage amplifier are contacted with the contact pads (shown in figure 4.1.) A 10 Hz triangular signal with a peak-to-peak voltage of approximately 3.2 V is applied to the voltage amplifier which amplifies this signal to an approximately 320 V peak-to-peak voltage. According to the established theory this causes a modulation of the polarisation state of the transmitted light. By setting a linear polarisation state at 45° to the $z$-axis (using the fibre polarisation-controller (FPC)) and putting a linear polariser at the output it is possible to convert the modulation of the polarisation state into an intensity modulation at the detector. Only one output from the PBS is tapped and thus it acts as a linear polariser.

The input fibre to the PBS (which is actually polarisation beam combiner used in reverse) is not polarisation maintaining [8]. This is unfortunate, but it is believed that any transformation of the polarisation state is small as the length of fibre is only 1 m long and it is not placed under any significant stress. Regardless, as was shown in section 2 the modulation voltage will be approximately the same regardless of rotation of the PBS, only the modulation depth and symmetry is affected.

Measurements on MZEOMs are carried out by exciting the waveguide with either TE or TM polarised light (set with the FPC) and applying a voltage to either a single arm or to both arms. In the case where only one arm is to be modulated, one of the probe needles connected to the voltage amplifier is elevated several millimetres above the device. The voltage is otherwise applied in the same fashion as for measurements using PMs.

As the theoretical treatment made clear, no external components are needed in order to achieve intensity modulation using the MZEOM structure. Thus, the output tapered fibre is connected directly to the infrared detector.

In both the case for PMs and MZEOMs, the oscilloscope records both the applied voltage $V$ and the voltage at the output of the signal amplifier. The voltage is assumed to be proportional to the measured intensity. Since many factors (such as losses in connectors, propagation losses and variable coupling efficency in and out of the device depending on alignment and local surface conditions) affect the total transmitted power, absolute measurements of intensity are regarded as unreliable. It is therefore useful to define

the normalised output intensity as

$$\frac{I}{I_{max}} = \frac{|V_{out}|}{|V_{out}|_{max}}, \tag{5.1}$$

where $V_{out}$ is the voltage measured at the output of the signal amplifier.

After normalisation of the output intensity, the obtained data looks somewhat like that shown in figure 5.3a. Here both the normalised output intensity $I/I_{max}$ and the applied voltage $V$ are plotted as functions of time $t$. However, in order to efficiently evaluate the electro-optic response of the device under test (DUT) it is better to use a plot such as the one in figure 5.3a, which presents the same data without the time component. In this plot the normalised output intensity is plotted as a function of the applied voltage. The fundamental data is the same as in figure 5.3a and each datapoint is simply the intensity/voltage coordinate at a single point in time. The colouring indicates whether or not the voltage is rising or falling at this point in time and facilitates the analysis of hysteresis. In the following section, all results will be presented on the same form as the latter plot.

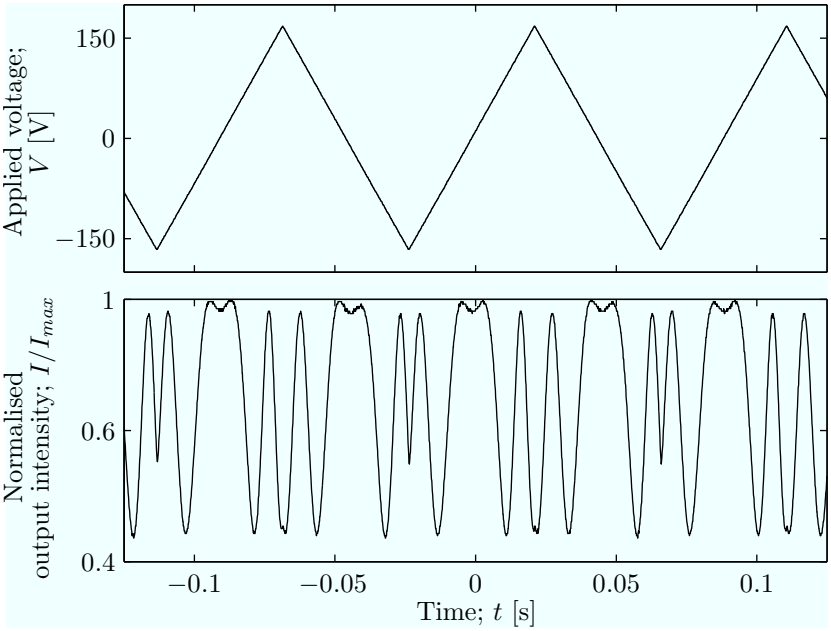


(a) The normalised output intensity (below) depends on the applied voltage (above). The output intensity is clearly asymetric depending on whether the applied voltage is rising or falling.

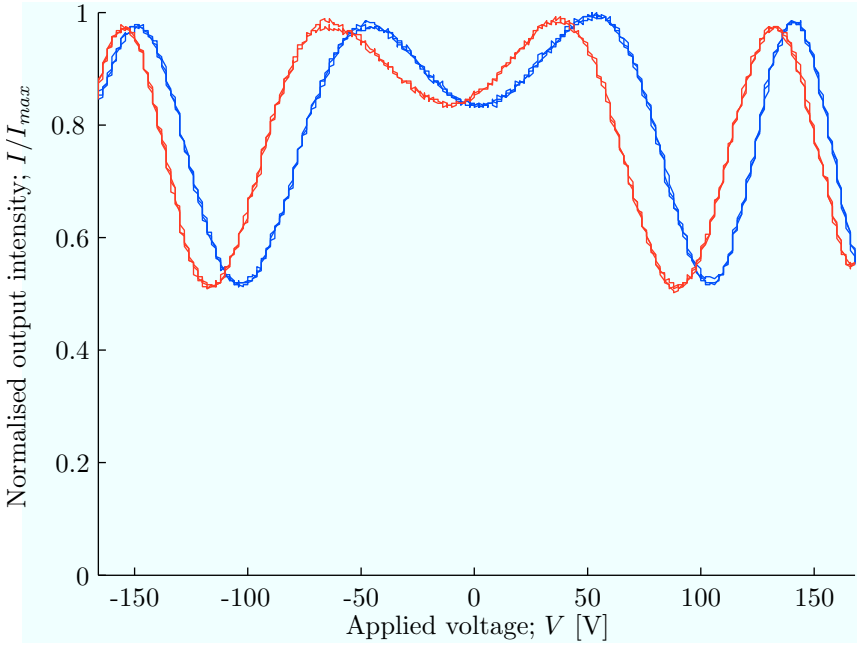


(b) The output intensity in figure 5.3a plotted as a function of the applied voltage in the same figure. Blue colour indicates an increasing voltage while red indicates a falling voltage, clearly showing hysteresis.

Figure 5.3: Example of typical plot used when presenting data.

# 6 Results and discussion

Several devices were manufactured and measurements made on them. Due to issues discussed in section 3.3 not all devices allowed measurements and on some devices only measurements with a single type of modulator was possible. In this section, measurments from four devices, numbered 1 through 4, are presented.

As stated in section 3, deviations in the ridge width $W$, electrode gap $d$ and etch depth $h$ are to be expected. Table 6 shows how the devices differ in actual geometric parameters, opposed to the ideal parameters. Since there are several possible values for $W$, the deviation $\Delta W$ from the ideal ridge width defined by the waveguide mask is given instead. In cases such as for $\Delta W$ for device 1 there is a variation across the entire device, this is probably caused by a non-uniform photoresist thickness.

Table 6: Measured geometrical parameters of fabricated waveguide devices.

| | $\Delta W$ [µm] | $d$ [µm] | $h$ [nm] |
|---|---|---|---|
| Device 1 | $\sim$0 to $\sim$0.5 | 8 | 55 |
| Device 2 | $\sim$0 | 7 | 160 to 200 |
| Device 3 | $\sim$0.5 | 8 | 55 |
| Device 4 | $\sim$0 | 8 | 100 to 130 |

For all devices except device 2 the deposited gold layer was 200 nm, while for device 2 it was 700 nm.

In order to evaluate the practicality of the modulators the first full modulation voltage $V_{ffm}$ is used. This voltage is rather loosely defined as the voltage required to go between a high intensity peak and deep intensity valley close to $V = 0$ V. A high peak and deep valley is loosely defined as a difference of approximately $70\% - 100\%$ of $I_{max} - I_{min}$.

## 6.1 Mach-Zehnder electro-optic modulators

Modulation of the output signal was achieved using the Mach-Zehnder electro-optic modulators (MZEOMs) on device 1 and 2. Significant differences were found between the two devices.

Figure 6.1 shows the results of typical measurements performed on device 1. The first, obvious observation is that there is significant and heavily distorted hysteresis when applying voltage to a single modulator arm; when voltage is applied to both arms the hysteresis is reduced significantly. It is interesting to observe that in the case of strong hysteresis the red curves are not simply

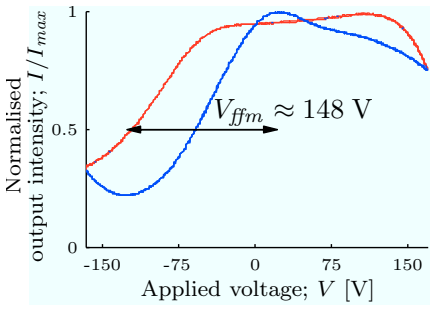


(a) TE polarisation. Modulation of one arm.

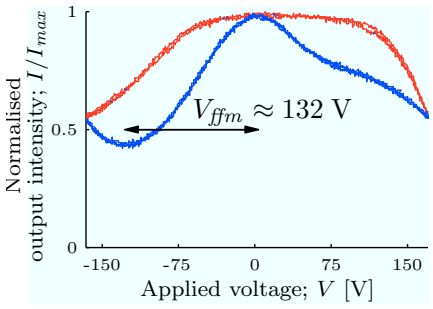


(b) TM polarisation. Modulation of one arm.

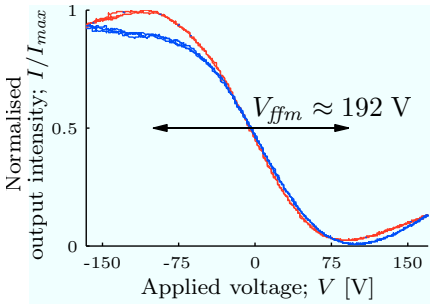


(c) TE polarisation. Modulation of both arms.

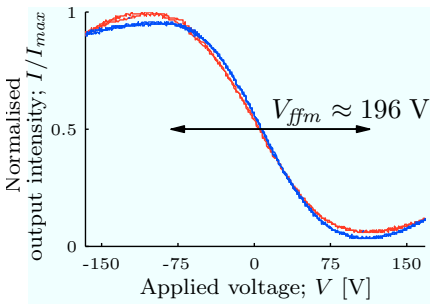


(d) TM polarisation. Modulation of both arms.

Figure 6.1: Typical responses for MZEOMs on device 1. All measurements are from MZ5.

the blue curves shifted by some amount. The 4mm point group, to which this thin film belongs, should have four fold rotational symmetry in the plane of the film; the same plane that the voltage is applied to. The properties of the material should follow the same symmetry making it unlikely that this strong asymmetry should be caused by some fundamental material property. Symmetric hysteresis is also expected based on the observations in PLZT [1].

One possible explanation is that there is some large, but finite resistance connecting the electrodes to other unconnected electrodes or spurious metal sites which allows charges to accumulate without providing a low impedance path for dischargin. Such added charges would create an additional electric field, superpositioned on the applied electric field. It is clear from figure 6.1 that the spurious hysteresis almost completely dissapears when the voltage is applied to both arms, suggesting that the effect is present, and approximately equal, in both modulator arms.

One possible site for charges to build-up is in a narrow metal ridge running alongside the metal electrodes. This metal ridge has been observed using atomic force microscopy (AFM) on device 1 and is shown in figure 6.2 which shows a height map of a single waveguide on device 1. However, AFM has not been applied to any other devices (which do not exhibit this kind of behaviour) and as such, no conclusion can be afforded as to whether the presented hypothesis is correct or not.

Another important observation is that contrary to expected results, no decrease is seen in $V_{ffm}$ can be observed when the voltage is applied to both arms as opposed to only a single arm; indeed, $V_{ffm}$ appears to increase. One possible explanation is that the dominant electro-optic effect is not the Pockels effect but rather the quadratic, Kerr effect. This effect stems from the third term in the Taylor expansion of the electro-optic effect which was presented in section 2.3. Since this effect is quadratic to the applied electric field it should be invariant to changes in the sign of the voltage which is the same as a change in direction of the applied voltage. Thus the effect in the two arms of an Mach-Zehnder electro-optic modulator (MZEOM) should cancel each other out. If this effect is dominant then the case where only a single arm is modulated (such as in figure 6.1a) then it would dominate over a weaker Pockels effect. However, when voltage is applied to both arm (such as in figure 6.1c) the Kerr effect would vanish, leaving only the Pockels effect. However, due to the not fully understood spurious hysteresis, the results of device 1 are not regarded as very reliable. Thus, no conclusion regarding the reason for the reduction in $V_{ffm}$ has been drawn.

Figure 6.3 shows the results of typical measurements performed on device 2. There are variations in shape between the measurements performed with TE and TM polarisation, but larger differences can be found within measurements with the same polarisation. Such variations have been found to

be caused by variation in alignment of the input and output fiber tapers and are believed to be caused by the coupling efficiency varying differently for different polarisations and modes. It is interesting to observe that even though the shapes differ slightly, the distances between peaks and valleys are approximately the same regardless of whether the polarisation is TE or TM.

Figure 6.3 also shows that the device exhibits hysteresis in all cases. Hysteresis is clearly strongest when modulating with two arms. This seems reasonable as each of the arms will exhibit hysteresis and increase the overall effect. Further examination of the figure reveals that the hysteresis is

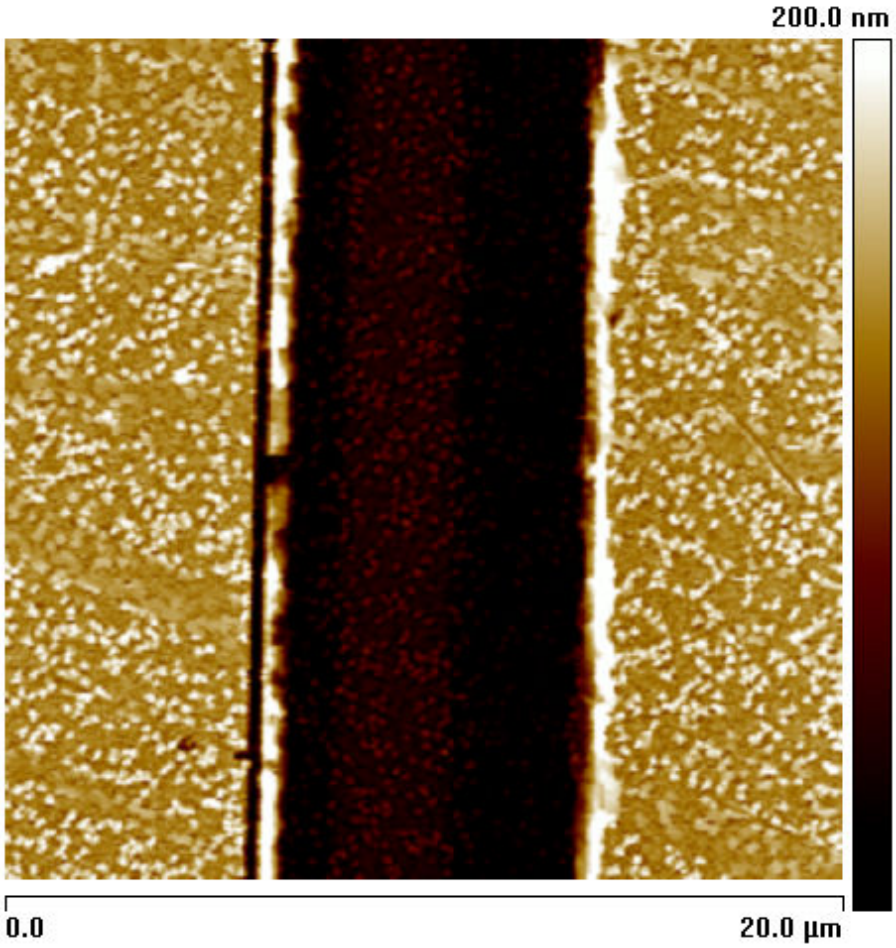


Figure 6.2: AFM measurement of waveguide with co-planar electrodes on device 1. The colour signifies the height of a point and the light areas are the electrodes while the darker areas are where the ridge-type waveguide is located. The waveguide is suggested with a slightly lighter shade.

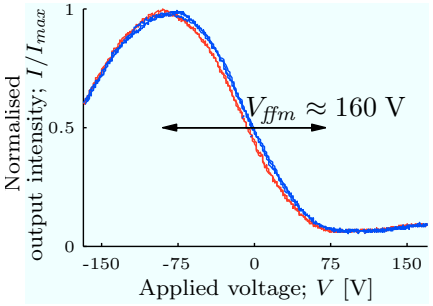


(a) TE polarisation. Modulation of one arm.

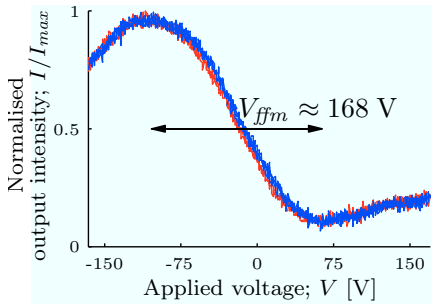


(b) TM polarisation. Modulation of one arm.

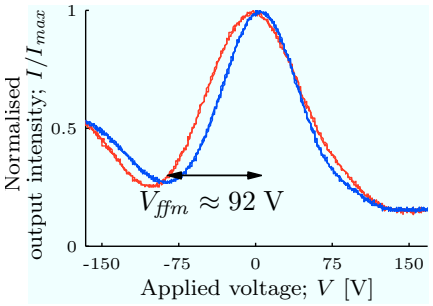


(c) TE polarisation. Modulation of both arms.

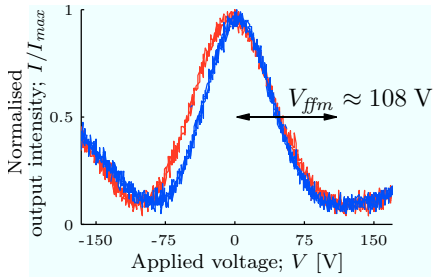


(d) TM polarisation. Modulation of both arms.

Figure 6.3: Typical responses for MZEOMs on device 2. All measurements are from MZ5.

asymmetrical. For example, in figure 6.3c the difference in intensity for a rising and falling voltage is much larger when the applied voltage is negative. Furthermore, comparing figure 6.3c with figure 6.3a indicates that the assymetry is inverted for measurements where only a single arm is modulated (ie, the difference in intensity is largest for positive voltages.) However, the trend is weak and the voltage range does not extend far enough into the negative to strongly conclude that this is a trend. This assymetry could indicate that there is some inherent polarisation in the material along the $a$-axis which adds to the electric field.

Contrary to the behaviour observed in device 1, device 2 shows a clear reduction in $V_{ffm}$ when voltage is applied to both arms of the MZEOM. This fits better with the established theory than an increase in $V_{ffm}$ and supports the theory that the observed electro-optic effect can be described as a Pockels effect.

## 6.2 Phase modulators

Modulation of the output signal was achieved using the phase modulators (PMs) on device 1, 3 and 4. Also here, significant differences were found between the devices.

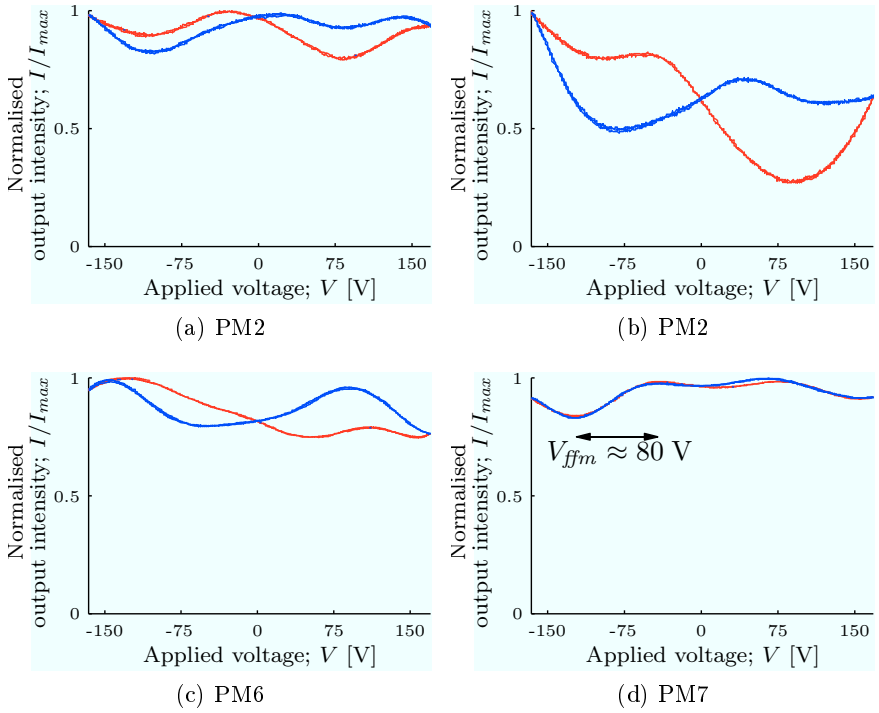


(a) PM2 (b) PM2

(c) PM6 (d) PM7

Figure 6.4: Typical responses for PMs on device 1.

Device 1 is of particular interest as it is the only device where successful measurements were achieved with both the MZEOMs and the PMs. Figure 6.4 shows some examples of typical results obtained from measurements on device 1's PMs. Similarly to the results obtained for the MZEOMs on device 1, significant hysteresis can be observed in the figures. As the figure shows, this spurious hysteresis makes it difficult to determine sensible values for $V_{ffm}$. However, there appears to be correlation between valleys and peaks between the different measurements.

Another observation is that the modulation depth is with few exceptions very poor. This can be be a result of poor input coupling leading to large amounts of light propagating in the thin film instead of the waveguide. This light would not be affected by the modulation voltage and would add a DC-level to the measured intensity. The fact that this effect does not appear to be very prominent in measurements using the MZEOMs on the same device can be explained by the fact that the PMs measurements were performed

several weeks after the MZEOMs measurements. During this time, surface defects and impurities could have been introduced through handling and cleaning. Both defects and surface impurities could lead to both increased scattering in the waveguide and increased coupling to the thin film.

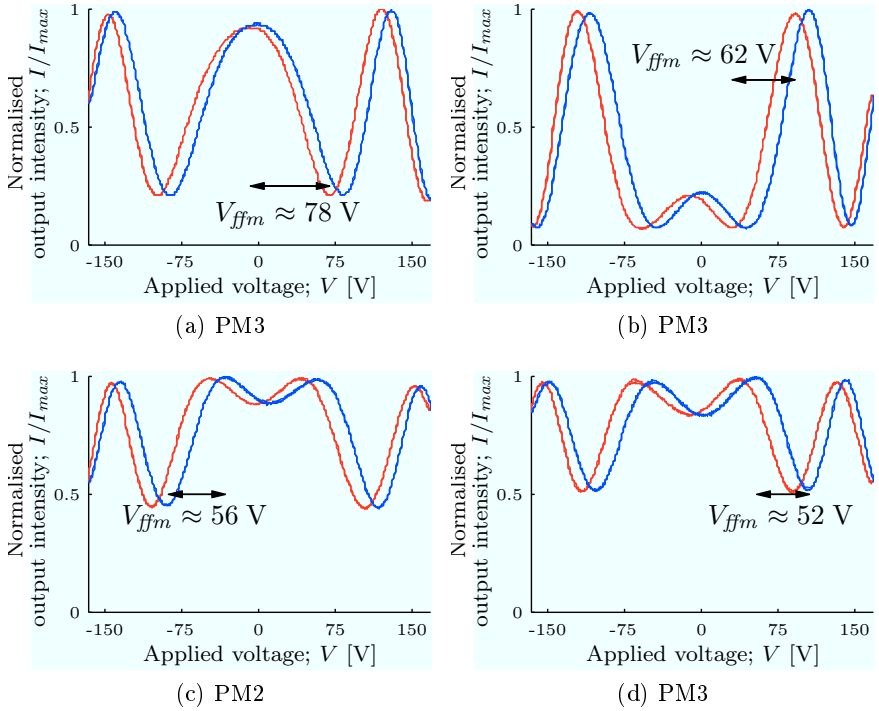


(a) PM3 (b) PM3

(c) PM2 (d) PM3

Figure 6.5: Typical responses for PMs on device 3. The two measurements on PM3 illustrates how the alignment of the input and output fibers can alter the response's shape and affect the value of $V_{ffm}$.

Figure 6.5 shows typical results of measurements on PMs on device 3. Good modulation was achieved with $V_{ffm}$generally on the order of 50 V. There is also a clearly defined hysteresis in all measurements. Even for a "well behaved" device such as this, comparison of figure 6.5a and figure 6.5b shows that alignment of the input and output fibers does affect the result. The central peak is clearly lower in the latter case and the side peaks appear at lower voltages. As demonstrated in section 2, this change in shape can be explained by an inherent phase change in the structure.

Figure 6.6 shows typical results of measurements on PMs on device 4. Compared to the other devices, it appears to exhibit significantly lower electro-optic effect. Comparing figure 6.6d with figure 6.6b reveals large variation in $V_{ffm}$; larger than for any other device. However, as discussed with regards to 3, the width of the central peak formation seems to be dependent on the alignment of the input and output fibres. Thus, for certain alignments, on a

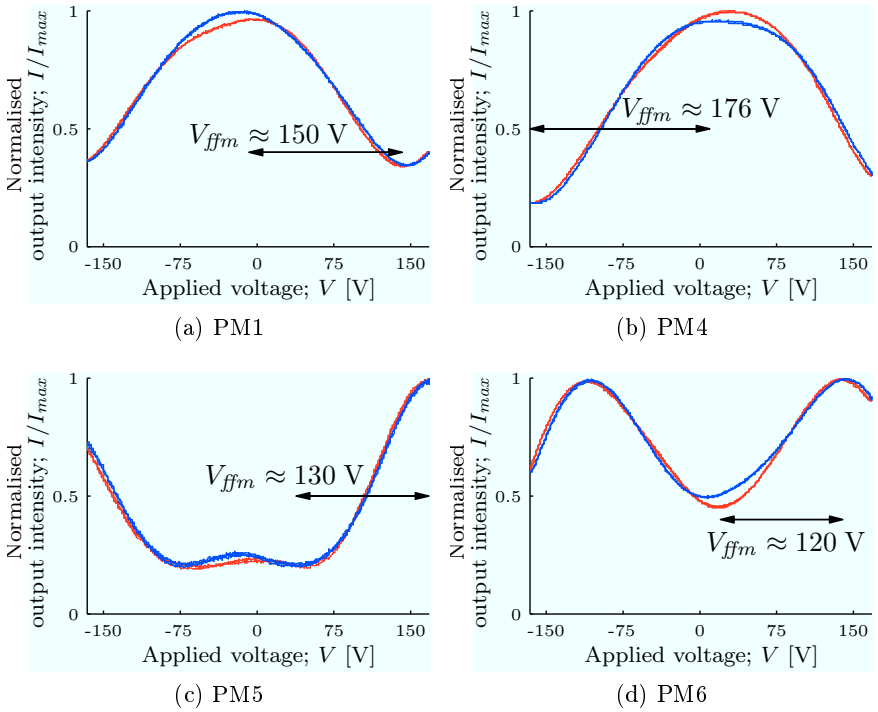


(a) PM1 (b) PM4

(c) PM5 (d) PM6

Figure 6.6: Typical responses for PMs on device 4.

device with low electro-optic effect, the central formation may extend close to the borders. For most other devices $V_{ffm}$ is not measured on slopes of the central peak formation, but on the neighbouring slopes. This illustrates that it is difficult to perform measurements of $V_{ffm}$ that are comparable between modulators.

One interesting observation on all three devices is that compared to figure 2.6 there appears to be no strong sloping in the response as the theory suggests for a polariser oriented with $\Theta \neq \pm\pi/4$ on the $z$-axis. This is best explained by accepting that $\Theta \approx \pm\pi/4$. However, this is not certain as the datasheet for the PBS [8] does not state the orientation of the input fiber with regards to the PBS's optical axis. Furthermore, the input fibre is, as previously mentioned, not polarisation maintaining and could potentially change the polarisation state of the output from the DUT. An alternative explanation could be that the observed effect can not be adequately explained by a model based on the Pockels effect or that there are some limitations in the assumptions made in the presented model. The primary suspect being the assumptions regarding the effect that the effective index ellipse is proportional to, and equally rotated as the index ellipse described by the bulk material properties.

## 6.3 Sources of distortion

Compared to the ideal simulations the measured response is distordted. This is particularly true for the results from MZEOMs

One obvious difference between the simulated and measured response can is that the voltage $V_{sym}$ about which the measured response is approximately symmetric is not $V = 0$ V as indicated by the proposed model. The measured response is rather (approximately) symmetric around some voltage offset from zero. The fact that the response "should" be symmetric around zero is obvious from the comparable simulation presented in section 2. It is also intuitive given that the perturbation of the refractive index as described by (2.12) and (2.14) is symmetric around zero. Since the perturbation of the refractive index is the fundamental macroscopic cause of the electro-optic effect it is obvious that the total response should also be symmetric. One possible explanation for the offset in $V_{sym}$ is that there exists an inherent electric field in the material due to ferroelectricity or that there a build up of a DC charge somewhere on or near the electrodes.

Another common distortion seen in particularly PMs lies in the shape around the symmetry point. Even for measurements on the same device modulator there can be large variations. This was illustrated by the difference between figure 6.5a and figure 6.5b which both presents successive measurements made with PM3 on device 3; the only difference between the measurements being the alignment of the tapered fibres. This can be explained by the fact that the light that is coupled into the waveguides is not exactly linearly polarised 45° on the $z$-axis due to the fact that the coupling coefficients for the TE and TM modes may vary. In addition, the material is inherently birefringent which means that the polarisation state will be altered before it enters the actual modulator between the electrodes. Since TE and TM polarized light, as used with the MZEOMs, is inherently parallel to the ordinary- and extraordinary-axis of the PLZT thin film, respectively, this birefringence effect will not have any great effect in MZEOMs.

The effect can be modelled by introducing an inherent phaseshift $\phi$ along one of the axes to the proposed model. Based on (2.29), the model for a PM then becomes

$$\boldsymbol{J}_{out} = R(-\Theta)T_{LP}(\Theta)T_R(\phi)R(-\theta)T_R R(\theta)\boldsymbol{J}_{in}, \tag{6.1}$$

where $T_R(\phi)$ is a retardation matrix as similar to that defined in (2.27). A similar modification of the MZEOM model can be adopted as there are differences in the phase of the waves propagating in each arm. For instance, figure 4.1 shows how an electrical conductor crosses one arm, but not the other. This perturbs the local refractive index and induces a phase difference.

## 6.4 Extraction of $V_{ffm}$

The responses presented for the four devices is only a representative subset of all the measurements that were performed. In order to evaluate the results, all measurements of $V_{ffm}$ have been combined into figure 6.7. In this figure, the measured values of $V_{ffm}$ are plotted as a function of the ridge width $W$. Each of the subplots represents one device with differing marks depending on the modulator type (PM or MZEOM) and the input polarisation state.

Comparing all the subplots, it is clear that there is great variation in the value of $V_{ffm}$ between devices. Figure 6.8a shows that the best performance was obtained using device 3, with $V_{ffm,min} = 46$ V as the lowest obtained modulation voltage. The results obtained from device 1, as shown in figure 6.7a, have a large variance. This is probably related to the previously discussed spurious hysteresis for this device. However, the results obtained from device 3 do indicate that $V_{ffm}$ is consitently lower for PMs than for MZEOMs. However, even if this is the case, the MZEOMs are preferred over the PMs when high integration is desired as the latter requires linear polarisers, which are difficult to create in highly integrated devices, to achieve intensity modulation. This is in contrast to the MZEOMs which are completely self contained intensity modulators.

Measurements on MZEOMs with applied voltage on both a single arm and both arms are contained in the results from device 1 in figure 6.7a and device 2 in figure 6.7b. These devices show contradictory behaviour. In device 1 $V_{ffm}$ is larger when voltage is applied to both arms than when voltage is applied to a single arm. In device 2, $V_{ffm}$ is largest when voltage is applied to a single arm. The latter result is as expected since each arm will impart an equal, but opposite, phase shift when voltage is applied to them. This doubles the total phase shift between light propagating in the two arms. For an MZEOM with $W = 3$ µm on device 2, the lowest measured $V_{ffm}$ goes from 160 V to 80 V when switching from modulation on a single arm to modulation on both arms. Even though this is only a single data point, it corresponds with the established theory and should be regarded as a good observation. As previously explained, this observation also confirms that the electro-optic effect is linear and not quadratic.

The results from device 1 and device 2 also confirm that there is no detectable difference in $V_{ffm}$ between TE and TM polarised light. This corresponds well with established theory.

The results obtained from PMs on device 3 suggest that $V_{ffm}$ depends on the ridge width $W$ with a measured increase of approximately 35% in $V_{ffm}$ between $W = 3.5$ µm to $W = 4.5$ µm. However, the results from the other devices do not show such a clear trend. Based on the established theory,

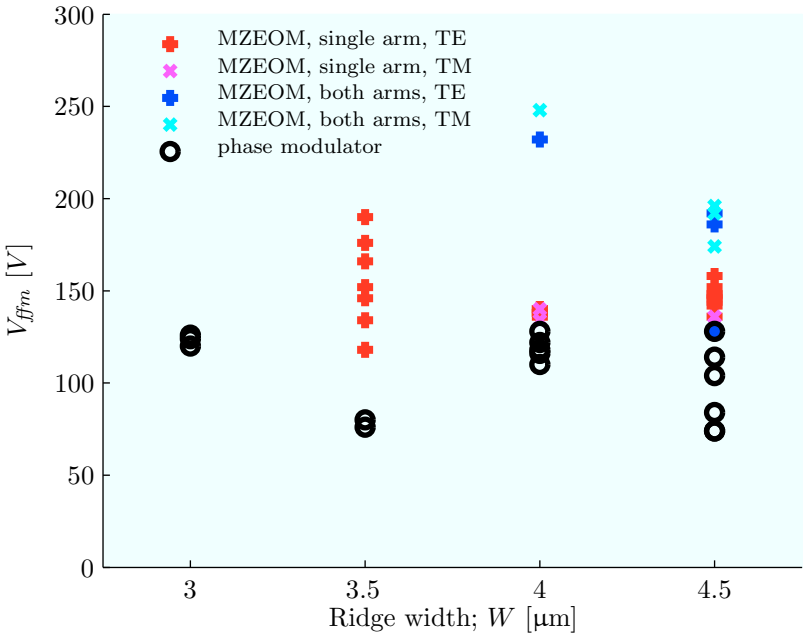


(a) Device 1

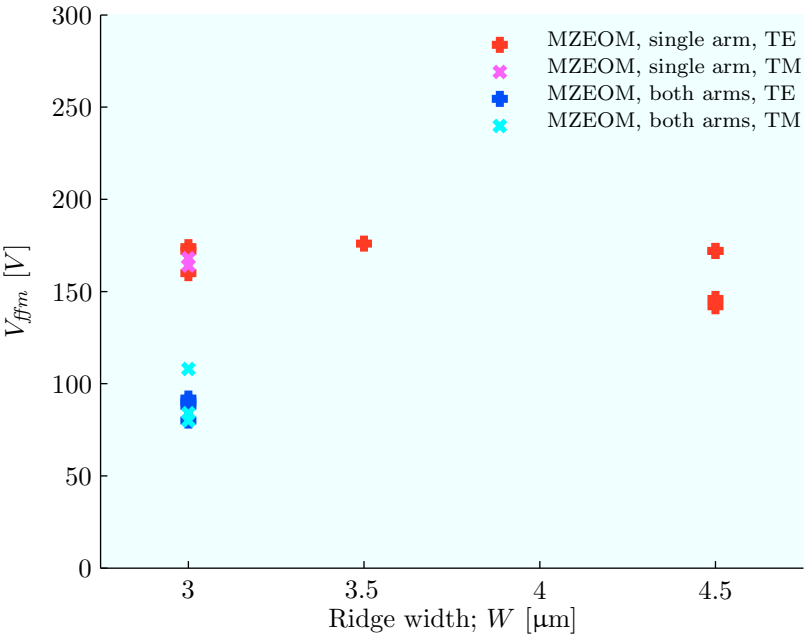


(b) Device 2

Figure 6.7: Measured $V_{fffm}$ for device 1 and device 2 as a function of ridge width $W$.

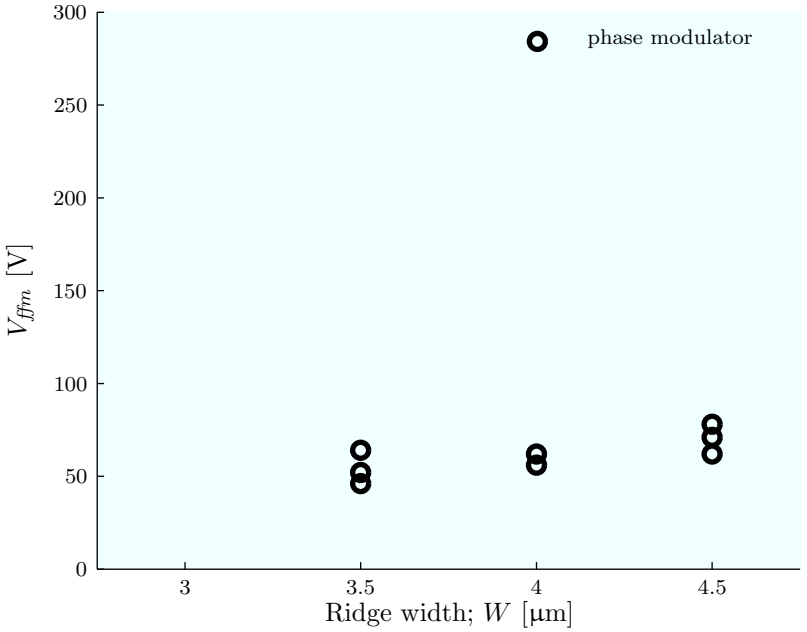


(a) Device 3

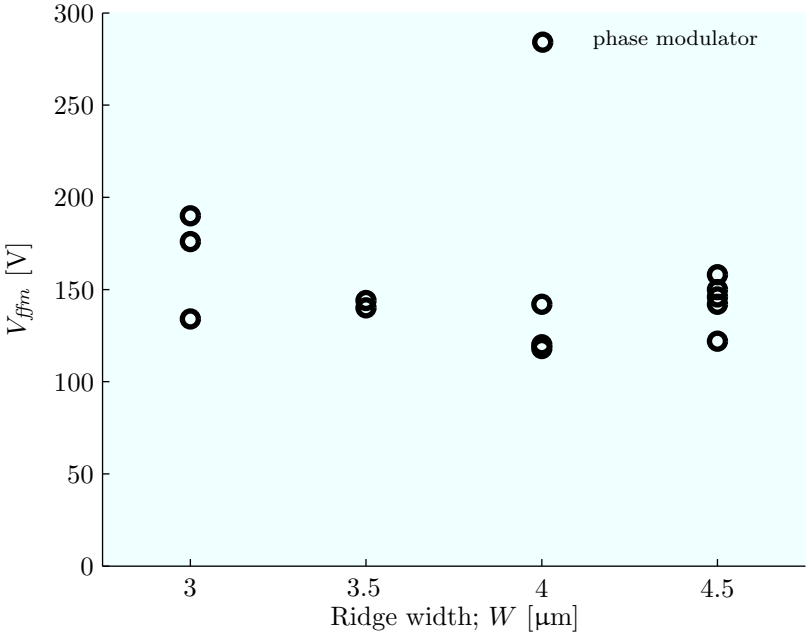


(b) Device 4

Figure 6.8: Measured $V_{ffm}$ for device 3 and device 4 as a function of ridge width $W$.

this dependency can be expected primarily on the basis that the effective refractive indices depend on the waveguide geometry. It is also plausible that a decrease in the overlap factor $\Gamma$ with decreasing ridge width $W$ (as the mode becomes less strongly confined) also contributes to an apparently weaker electro-optic effect. Overall, however, the results do not afford any conclusion with regards to the ridge-width dependence of $V_{\pi m}$, but it is a point of interest for further investigations.

## 6.5 Extraction of $\mathfrak{r}_{51}$

In order to evaluate the model for the electro-optic effect given in section 2, some assumptions have to be made with regards to the value of certain variables. Values for $\Gamma$, $C_{TE0}$ and $C_{TE0}$ have been previously established in section 2. The geometrical parameters were given in table 5. There is some uncertainty in the values of the material parameters. The refractive index of $c$-oriented epitaxial 8/40/60 PLZT thin films on MgO is reported to be $n \approx 2.45$. The birefringence of bulk 8/40/60 PLZT has reported to be $\Delta n \approx 0.00125$ [1]. However, the fabricated bulk PLZT is not single crystal and it is reasonable to assume that the birefringence of high quality, mono crystalline PLZT is higher. Although no data for epitaxial 8/40/60 PLZT has been found, both [9] and [10] reports measured values of $\Delta n$ in epitaxial 8/65/35 PLZT. The former article reports $\Delta n$ as 0.002 in thin-films epilayers on Nb doped $SrTiO_3$ while the latter article reports $\Delta n$ as high as 0.01 for thin-film epilayers on on sapphire. As a comparison, [1] reports $\Delta n$ as high as 0.008 for the same composition, but in bulk. This indicates that there are many unknown factors which affect $\Delta n$ in thin films. However, under the assumption that the argument of mono crystalline PLZT thin-films having a larger $\Delta n$ than bulk PLZT holds, a very rough estimate of $\Delta n \approx 0.005$ is used for calculation of $\mathfrak{r}_{51}$.

In order to extract approximate values for $\mathfrak{r}_{51}$, a curve fitting technique was employed. The theoretical model given by in (6.1) has been fitted to selected measurements from PMs on device 1, 3 and 4. The PMs were chosen due to their general "good behaviour" and a smaller number of unknowns compared to the model for the MZEOMs. The curve fitting was performed assuming that the polarisation state of the input light can be described by the Jones vector

$$J_{in} = \frac{1}{\sqrt{2}} \begin{bmatrix} 1 \\ 1 \end{bmatrix}. \tag{6.2}$$

Furthermore, as previously discussed, other factors external to the proposed model can affect the modulation depth. As a consequence, the modulation depth has been assumed to be 100% for all cases. Also, the curve fitting does not account for hysteresis and for each dataset only one of the customarily

red and blue curves have been chosen for curve fitting. The curve fitting was performed with the MATLAB script listed in appendix D. This scripts fits a simulated response with the average measured response by finding a local minimum to the error function

$$e = \sqrt{\sum_{i=N} \left(I_i' - I_i^{ideal}\left(\mathfrak{r}_{51}, \phi, \Theta\right)\right)^2}, \tag{6.3}$$

where $I'$ is the measured, normalised output intensity with 100% modulation depth, $I_{ideal}\left(\mathfrak{r}_{51}, \phi, \Theta\right)$ is the modelled output intensity based on (6.1) and $N$ is the number of samples in the measured intensity. As (6.3) shows, the data is fitted with regards to $\mathfrak{r}_{51}$, $\phi$ and $\Theta$. However, for device 3 and device 4 the value of $\Theta$ was kept fixed at $\pi/4$. In order to account for the apparent offset of the symmetry voltage in the measured output intensity, an offset voltage is manually added to the voltage used for modelling the response, aligning the symmetry voltage of the measured intensity with the modelled intensity.

Using the aforementioned method, excellent fits were achieved as shown in figure 6.9, figure 6.10 and figure 6.11. (Appendix B completes the set of curve fitting plots.) In these plots, the measured data is indicated alongside the average of the measured data to which the model is fitted. The figures shows that the curves can be fitted very well, particularly with regards to matching peaks and valleys. Large variation in $\phi$ are observed, however as it is mostly attributed to alignment the values are not reported. Regarding $\Theta$, curve fitting performed on data from device 1 resulted in a $\Theta \approx 1.1$ rad, which is a 42% deviation from the ideal $\Theta = \pi/4$. Though large, it is not suprising when considering the generally spurious response (particullary with regards to hysteresis.) The deviation could also be explained by variations in the setup resulting in a change in output polarisation state.

The complete set of results from all curve fittings is listed in table 7. This table confirms the trends observed for $V_{ffm}$ and generally gives 11 pm/V as a maximum estimate for the observed value of $\mathfrak{r}_{51}$.

When considering these data it is important to remember that there is a large uncertainty associated with the birefringence $\Delta n = |n_o - n_e|$. For PM3 on device 3, changing $\Delta n$ and rerunning the curve fitting script, clearly shows that the estimate for $\mathfrak{r}_{51}$ is strongly dependent on $\Delta n$. This is shown in table 8.

The subjective evaluation of the curve fit in shape and modulation depth suggests that perhaps $\Delta n \approx 0.005$ is too large an estimate and that a better estimate could be found closer to $\Delta n \approx 0.00125$.

The approximation of $\mathfrak{r}_{51}$ does also rely on other approximations such as that of the electric field and the effective refractive indices. However, except for the unknown effect of the geometrical parameters of the waveguide, these

Table 7: Estimated values of $\mathfrak{r}_{51}$. Figures in text and appendix show curve fit.

| | Modulator | $\mathfrak{r}_{51}$ [pm/V] (numeric fit) | |
|---|---|---|---|
| Device 1 | PM1 | 8.5 | Figure 6.9 |
| | PM7 | 7.6 | Figure B.1 |
| Device 3 | PM1 | 10 | Figure 6.10 |
| | PM2 | 11 | Figure B.2 |
| | PM3 | 11 | Figure B.3 |
| Device 4 | PM2 | 4.7 | Figure B.4 |
| | PM4 | 4.8 | Figure 6.11 |
| | PM5 | 6.1 | Figure B.5 |
| | PM6 | 5.8 | Figure B.6 |
| | PM7 | 4.4 | Figure B.7 |

Table 8: Dependence of $\mathfrak{r}_{51}$ on $\Delta n$ when performing curve fitting.

| $\Delta n$ | $\mathfrak{r}_{51}$ [pm/V] (numeric fit) |
|---|---|
| 0.00125 | 5.9 |
| 0.005 | 11 |
| 0.01 | 15 |

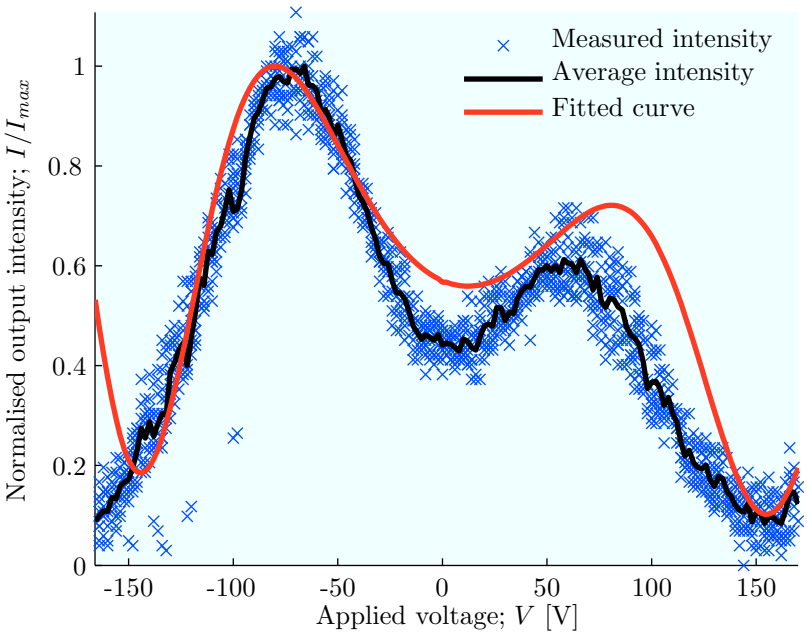


Figure 6.9: Curve fitting for device 1, PM1: $\mathfrak{r}_{51} \approx 8.5$ pm/V.

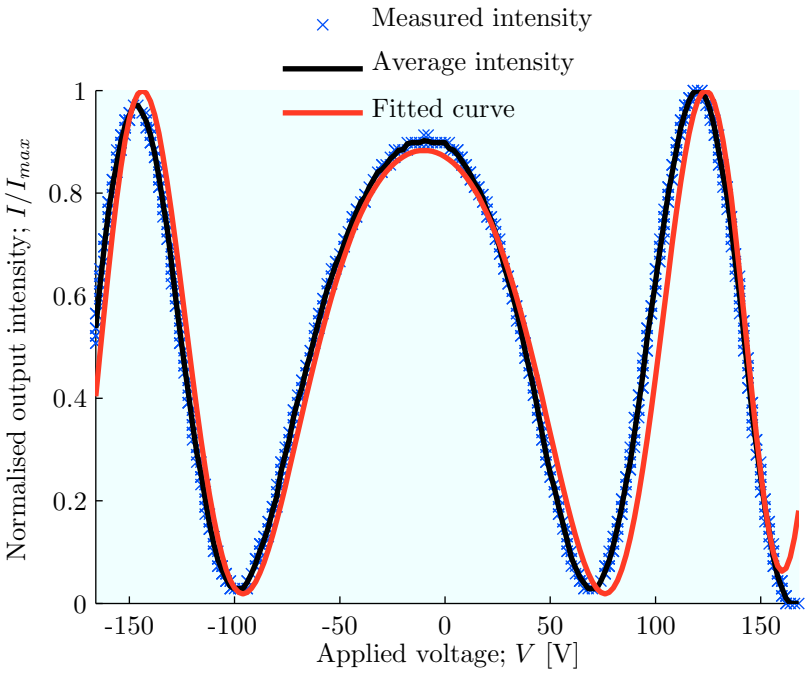


Figure 6.10: Curve fitting for device 3, PM1: $r_{51} \approx 10$ pm/V.

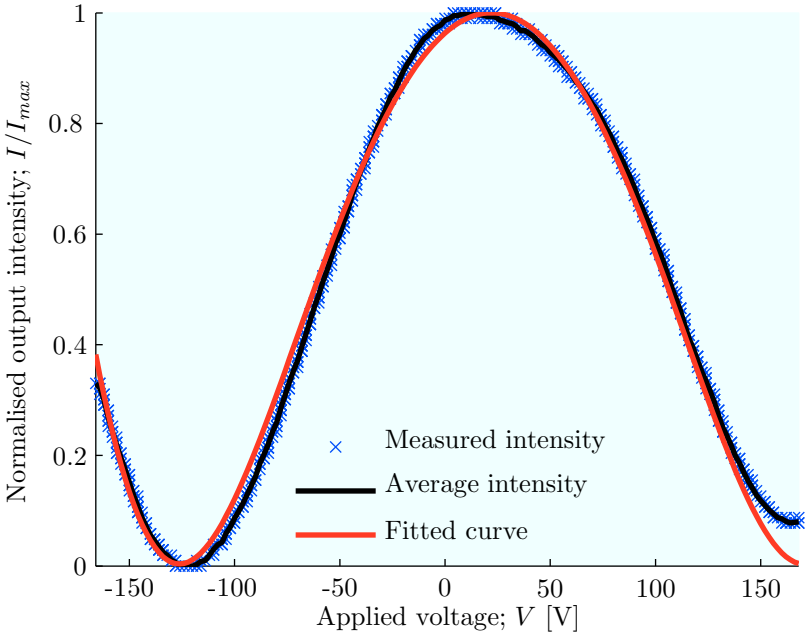


Figure 6.11: Curve fitting for device 4, PM4: $r_{51} \approx 4.8$ pm/V.

effects should only affect $\mathfrak{r}_{51}$ linearly. Looking back at (2.11), (2.12) and (2.14) it is clear that it is actually the product

$$\mathfrak{r}_{51}\frac{V}{d}\Gamma \tag{6.4}$$

which has been discovered through curve fitting. $V$ and $d$ are well known quantities, but it is clear that any deviation from the estimated value of $\Gamma \approx 0.88$ will affect the estimate for $\mathfrak{r}_{51}$

## 6.6 Comparison of measured $\mathfrak{r}_{51}$ with expected value

The approximated values for $\mathfrak{r}_{51}$ are significantly smaller than what was to be expected. Values for an effective Pockels coefficient on the order of $\sim 10^2$pm/V have been reported [1].

One explanation for the reduction of the Pockels coefficient can be attributed to the multidomain nature of perovskite oxides where the unit cell of the crystal lattice can be either polarised up or down along the $c$-axis [11]. In an unpoled material the distribution of the two types of domains will be the result of a stochastic process [11]. It has been suggested in [12] that the effective non-linear electrical properties are reduced by an amount proportional to the difference in area covered by different polarisation directions. In the case of the $\mathfrak{r}_{51}$ coefficient, [13] has shown that based on the previously mentioned theory, the efficient Pockels coefficient $\mathfrak{r}_{51}^{eff}$ (which is what has been measured) is given by

$$\mathfrak{r}_{51}^{eff} = D^c\mathfrak{r}_{51}, \tag{6.5}$$

where $D^c$ is the difference in the relative area of domains polarised in opposite directions along the $c$-axis.

It is reasonable to assume that the film taken "as grown" will be multi domain and piezo force microscopy (PFM) were performed in order to confirme this. Unfortunately, due to the co-planar nature of the electrodes and unknown residual particles on the surface, it was not possible to obtain a conclusive measurement.

Due to the probable stochastic distribution of the domains $D^c$ is expected to vary between thin films; which could explaine the observed variation in $V_{ffm}$ and $\mathfrak{r}_{51}$ between devices.

## 6.7 Other observations

A few other observations have been made with regards to the performance of the electro-optic modulators. Among others, it is observed that in general the

absolute voltage amplitude of the measured signal is weaker for TM modes than for TE modes. This is believed to be due to the fact (as mentioned in section 2) that TM modes are guided more weakly than TE modes. This causes the mode to occupy a larger space than and as a consequence have larger overlap with the air/PLZT interface; scattering at this interface is believed to be an important loss mechanism.

Though the modulation depth has not been investigated thoroughly, the presented figures suggest that $\sim$75% modulation is easily achievable and figure particularly shows that $\sim$100% modulation can be achieved. The variation in modulation depth is believed to be mostly related to the alignment of fibre and light guided in the thin-film or substrate as a whole.

It is also observed that in most cases a relatively high DC bias (on the order of tens of volts) is required in order to operate the modulators in the linear region. This is disadvantageous for practical modulator devices. Combined with the relatively high values for $V_{ffm}$ the devices do not seem to be suitable for use as practical electro-optical modulators as is. This could be alleviated by increasing the interaction length $L$ or creating single domain films as suggested in section 6.6.

# 7 Conclusion

This work has shown that it is possible to fabricate electro-optic modulators in 500 nm thick $c$-axis oriented epitaxial $(Pb_{0.92},La_{0.08})(Zr_{0.4},Ti_{0.6})O_3$ thin films on MgO substrate using a common photolitography, wet etching and lift-off metallisation process. The modulator design has been based on ridge type waveguides and co-planar gold electrodes with an interaction length $L = 3$ mm. Several devices with both Mach-Zehnder electro-optic modulators and phase modulators have been successfully fabricated and polishing the end faces of the fabricated devices has been shown to facilitate coupling of light into the waveguide.

he lowest practical modulation voltage achieved with a Mach-Zehnder electro-optic modulator is reported to be $V_{ffm} \approx 80$ V applied to both arms of the modulator. For phase modulators with a linear polariser at the output, the lowest achieved modulation voltage is reported to be $V_{ffm} \approx 46$ V. Significant difference in $V_{ffm}$ is found between each device.

A model based on Jones matrix formalisms and the assumption that the electro-optic effect is primarily a Pockels effect has been proposed for both phase modulators and Mach-Zehnder modulators. Curve fitting of the model with measured electro-optic responses made on phase modulators have been performed. The obtained fits match well with the measured intensity and indicate that the model is sound. The fits also indicate that while the Pockels coefficient was found to be approximately constant for each device, large differences were found between devices. The estimates for $\mathfrak{r}_{51}$ range from 4.4 pm/V to 11 pm/V. The approximated values are found to be strongly dependent on the birefringence of PLZT which was assumed to be $\Delta n \approx 0.005$. This assumption is believed to be weak and it is suggested that $\Delta n$ is actually lower, causing the estimates of $\mathfrak{r}_{51}$ to decrease.

The estimated values for the Pockels coefficient are much lower than the expected value of $\mathfrak{r}_{51} \sim 10^2$ pm/V. It has been suggested that this is related to the PLZT thin film being multi domain. This is also believed to be the cause of the variation in $\mathfrak{r}_{51}$ between devices as the domain distribution is believed to be the result of a stochastic process.

# 8 Suggested future work

Due to the inherent nature of a master thesis, time constraints limits the amount of work that can be performed within the project. This section gives some suggestions on some of what could have been done, given an unlimited time frame.

No theoretical treatment has been found on the effect of a rotating index ellipsoid in ridge-type waveguides. It would be interesting to investigate how the waveguide geometry affects the rotation of an effective index ellipsoid related to a propagating mode. In general it would be interesting to explore more in depth how the waveguide geometry affects the effective refractive index with regards to the Pockels effect and whether or not any correlation can be expected between the modulation efficiency represented by $V_{ffm}$ and the geometrical parameters $W$ and $h$.

In order to facilitate accurate design of electro optical modulators in $c$-oriented PLZT on MgO with different wavguide geometry it is necessary to know the physical values of the Pockels tensor $\mathfrak{r}_{ij}$. As this project has shown, theoretical models can be constructed that fit the measured data, but it is necessary to know several physical properties of the material and waveguide structure in order to extract an accurate value for $\mathfrak{r}_{51}$. The variable that is associated with the greatest uncertainty is the birefringence $\Delta n = |n_e - n_o|$. It should be possible to measure this independent of $\mathfrak{r}_{51}$ by using a method similar to that in [9]. Comparison with a model based on both the Pockels and Kerr effect would also be interesting.

As an alternative, re-performing curve fitting with $\Delta n$ as a free variable and paying closer attention to the modulation depth and shape could reveal a more exact estimate of $\mathfrak{r}_{51}$ while also providing an estimate for $\Delta n$.

As the measured Pockels coefficient is lower than what was expected it would be interesting to investigate the source of this. A starting point has been suggested in section 6.6 and it should be possible to confirm the basic premise of the theory by redoing the experiment with poled PLZT thin films.

The experiments have also shown clear hysteresis along the $a$-axis and it would be interesting to add this effect to the proposed model in order to measure the hysteresis loop.

# A Diagonalisation of impermeability tensor

The impermeability tensor $\eta_{ij}(E)$ given by (2.10) can be considerd equivalent to the matrix

$$M = \begin{bmatrix} A & 0 & C \\ 0 & A & 0 \\ C & 0 & B \end{bmatrix}. \tag{A.1}$$

This matrix exists in the $xyz$ coordinate system, but it can also be represented as a diagonal matrix $M'$ in a transformed $x'y'z'$ coordinate system; this is acheived using eigen decomposition.

The eigenvalues $\lambda$ of $M$ are given by

$$\det(M - \lambda I) = 0, \tag{A.2}$$

which becomes

$$\det \begin{vmatrix} A-\lambda & 0 & C \\ 0 & A-\lambda & 0 \\ C & 0 & B-\lambda \end{vmatrix} = 0 \tag{A.3}$$

$$(A-\lambda)(A-\lambda)(B-\lambda) - C(A-\lambda)C = 0 \tag{A.4}$$

$$(A-\lambda)((A-\lambda)(B-\lambda) - C^2) = 0. \tag{A.5}$$

It is obvious that (A.5) has three solutions and that $\lambda = A$ is one of them. The two others are given by

$$(A-\lambda)(B-\lambda) - C^2 = 0 \tag{A.6}$$

$$\Downarrow \tag{A.7}$$

$$\lambda^2 - (A+B)\lambda + AB - C^2 = 0, \tag{A.8}$$

which is a common quadratic equation with the solution

$$\lambda = \frac{1}{2}\left(A + B \pm \sqrt{(A-B)^2 + 4C^2}\right). \tag{A.9}$$

Thus, the eigenvalues of the $M$ in (A.1) are

$$\lambda_1 = \frac{1}{2}\left(A + B + \sqrt{(A-B)^2 + 4C^2}\right) \tag{A.10}$$

$$\lambda_2 = A \tag{A.11}$$

$$\lambda_3 = \frac{1}{2}\left(A + B - \sqrt{(A-B)^2 + 4C^2}\right). \tag{A.12}$$

The three eigenvectors of $M$ in the form $\boldsymbol{X}_i = [x_{i1}, x_{i2}, x_{i3}]^T$, where $i \in \{1, 2, 3\}$, are given by

$$M\boldsymbol{X}_i = \lambda_i \boldsymbol{X}_i \qquad \text{for} \quad i = \{1, 2, 3\} \tag{A.13}$$

$$\begin{bmatrix} x_{i1}A + x_{i3}C \\ x_{i2}A \\ x_{i1}C + x_{i3}B \end{bmatrix} = \lambda_i \begin{bmatrix} x_{i1} \\ x_{i2} \\ x_{i3} \end{bmatrix} \quad \text{for} \quad i = \{1, 2, 3\} \tag{A.14}$$

For $i = 2$, the first and third terms are only satisfied in general for $x_{21} = x_{23} = 0$. $x_{22}$ is satisfied for any value except 0, which would be a trivial solution. For $i = 1$ and $i = 3$, (A.13) gives $x_{i2} = 0$ while $x_{i1}$ and $x_{i2}$ are given by

$$x_{i1} = \frac{1}{2C}\left(A - B \pm \sqrt{(A-B)^2 + 4C^2}\right) x_{i3} \tag{A.15}$$

$$x_{i3} = \frac{1}{2C}\left(B - A \pm \sqrt{(A-B)^2 + 4C^2}\right) x_{i1}. \tag{A.16}$$

Depending on the choise of value for either $x_{i1}$ or $x_{i3}$ and the choise of sign the coordinate system can be rotated $\pm 90°$ or $180°$. Choosing $+$ for $i = 1$, $-$ for $i = 3$, and $x_{13} = x_{31} = 1$ in (A.15) gives easily interpreted results; the eigenvectors then becomes

$$\boldsymbol{X}_1 = \begin{bmatrix} 1 \\ 0 \\ \frac{1}{2C}\left(B - A + \sqrt{(A-B)^2 + 4C^2}\right) \end{bmatrix} \tag{A.17}$$

$$\boldsymbol{X}_2 = \begin{bmatrix} 0 \\ 1 \\ 0 \end{bmatrix} \tag{A.18}$$

$$\boldsymbol{X}_3 = \begin{bmatrix} -\frac{1}{2C}\left(B - A + \sqrt{(A-B)^2 + 4C^2}\right) \\ 0 \\ 1 \end{bmatrix}. \tag{A.19}$$

Being eigenvectors, $\boldsymbol{X}_1$, $\boldsymbol{X}_2$ and $\boldsymbol{X}_3$ are orthogonal and parallel to the principal axes $x'$, $y'$ and $z'$ of $M$. Since $\boldsymbol{X}_2$ is parallel with the $y$-axis and $\boldsymbol{X}_1$ and $\boldsymbol{X}_3$ are orthogonal, it is obvious that $M$ is diagonalized by rotating the system a certain angle $\theta$ around the $y$-axis. Figure A.1 shows how the rotated $x'y'z'$ coordinate system relates to the $xyz$ coordinate system. The figure also clearly show that the rotation is given by

$$\begin{aligned} \theta &= \arctan\left(-\frac{x_{31}}{x_{33}}\right) = \arctan\left(\frac{x_{13}}{x_{11}}\right) \\ &= \arctan\left(\frac{1}{2C}\left(B - A + \sqrt{(A-B)^2 + 4C^2}\right)\right). \end{aligned} \tag{A.20}$$

By comparing this equation with (A.10) and (A.12) it becomes clear that it is possible to rewrite the eigen values as

$$\lambda_1 = A + C\tan\theta \tag{A.21}$$
$$\lambda_2 = A \tag{A.22}$$
$$\lambda_3 = B - C\tan\theta \tag{A.23}$$

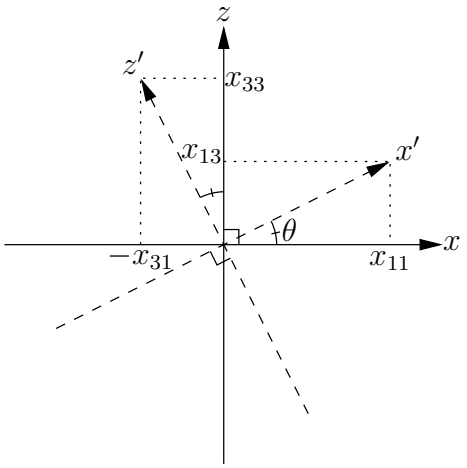


Figure A.1: The geometrical relation between the $xz$-plane and the rotated $x'z'$-plane. The $y'$-axis coincides with the $y$-axis.

Finally, the diagonalized matrix $M'$ is given by

$$\begin{aligned} M' &= \begin{bmatrix} \lambda_1 & 0 & 0 \\ 0 & \lambda_2 & 0 \\ 0 & 0 & \lambda_3 \end{bmatrix} \\ &= \begin{bmatrix} A + C\tan\theta & 0 & 0 \\ 0 & \lambda_2 & A \\ 0 & 0 & B - C\tan\theta \end{bmatrix} \end{aligned} \tag{A.24}$$

# B Curve fitting

The following figures shows the result of curve fitting produced by the code in listing

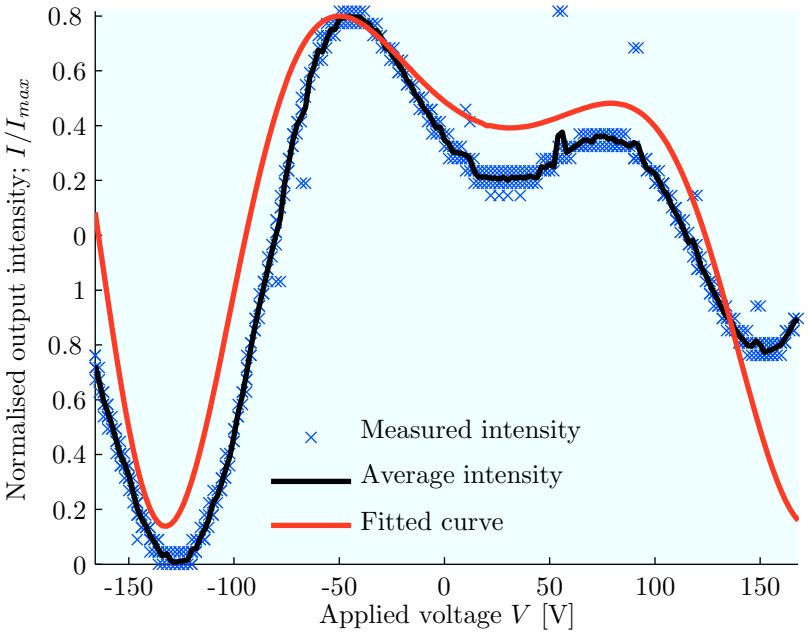


Figure B.1: Curve fitting for device 1, PM7: $\mathfrak{r}_{51} \approx 7.6$ pm/V.

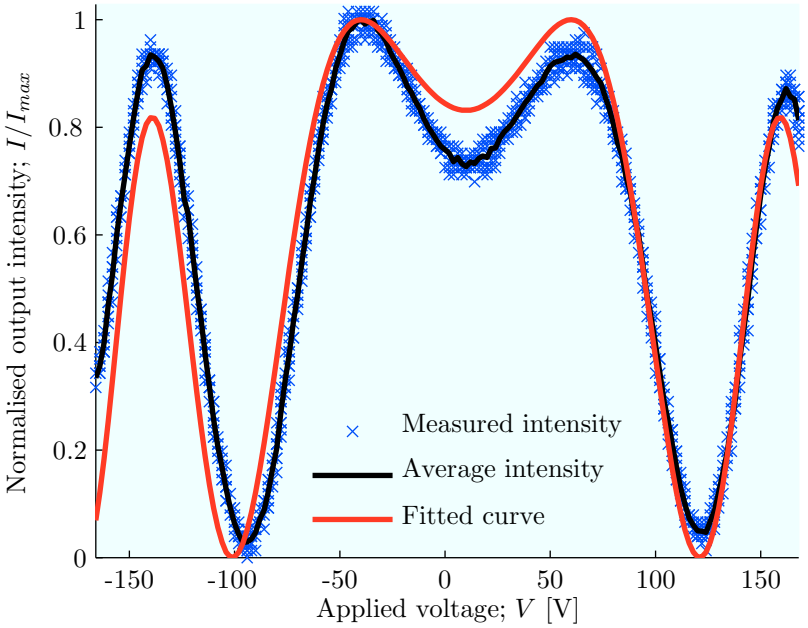


Figure B.2: Curve fitting for device 3, PM2: $\mathfrak{r}_{51} \approx 11$ pm/V.

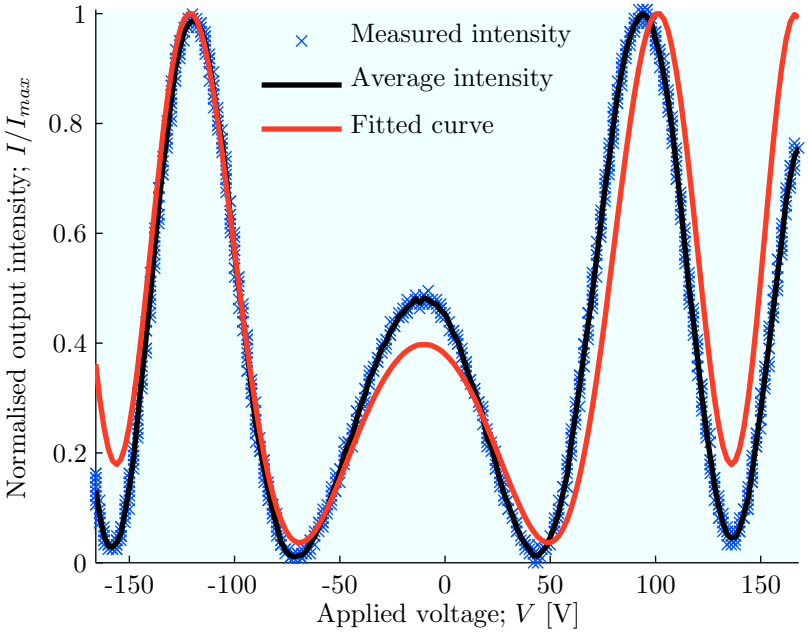


Figure B.3: Curve fitting for device 3, PM3: $\mathfrak{r}_{51} \approx 11$ pm/V.

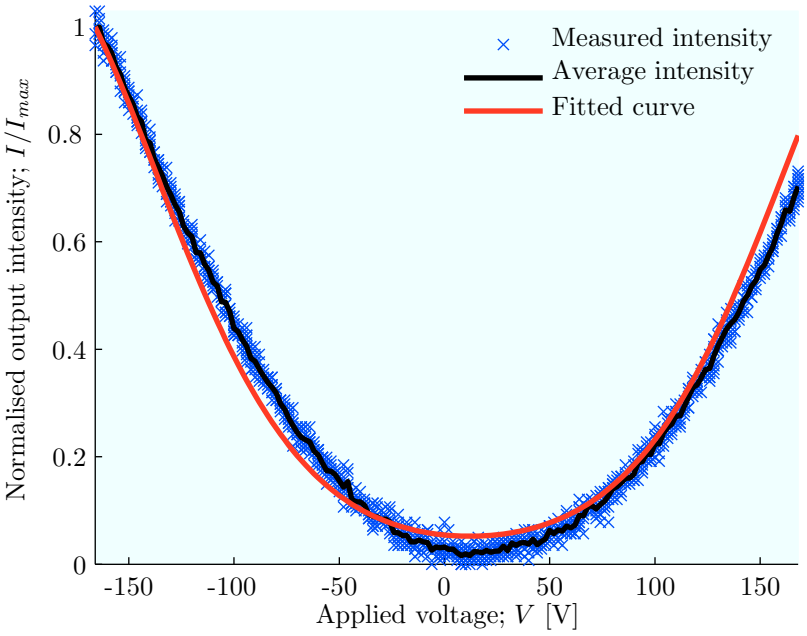


Figure B.4: Curve fitting for device 4, PM2: $\mathfrak{r}_{51} \approx 4.7$ pm/V.

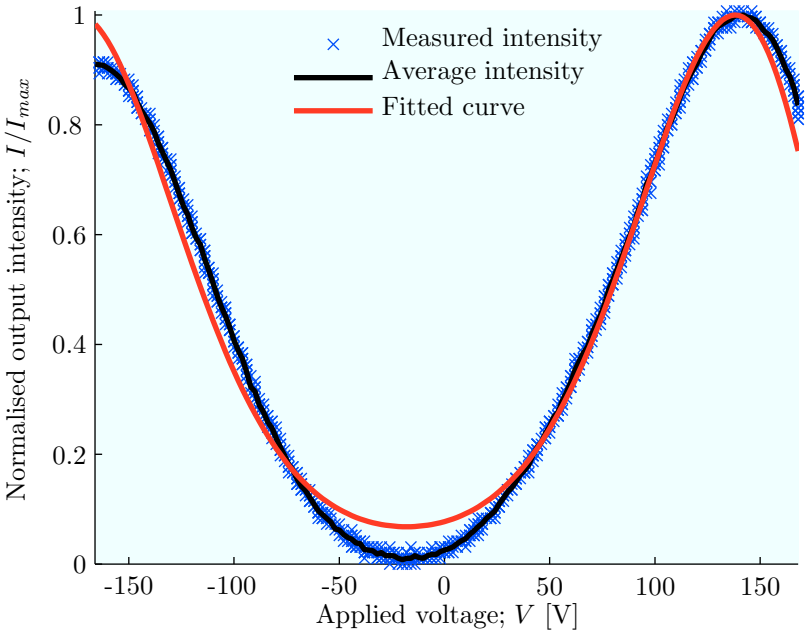


Figure B.5: Curve fitting for device 4, PM5: $\mathfrak{r}_{51} \approx 6.1$ pm/V.

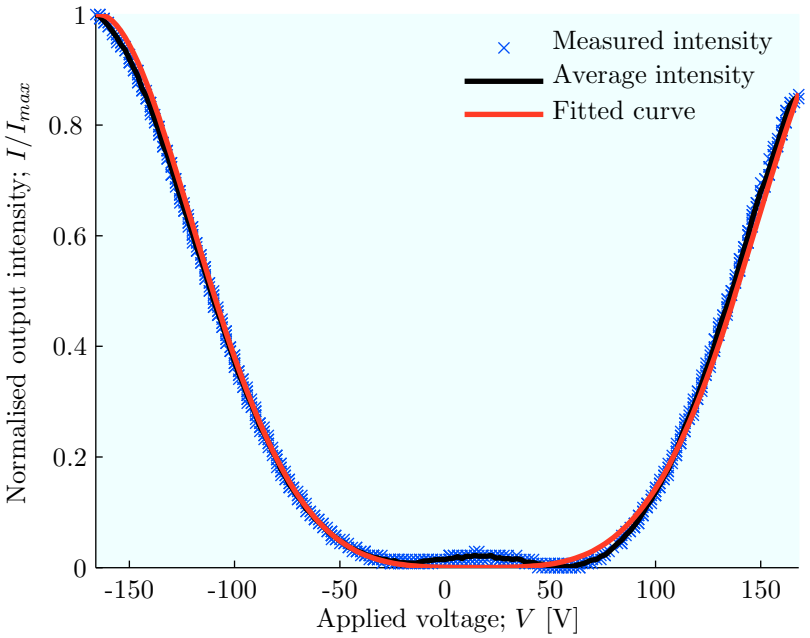


Figure B.6: Curve fitting for device 4, PM6: $\mathfrak{r}_{51} \approx 5.8$ pm/V.

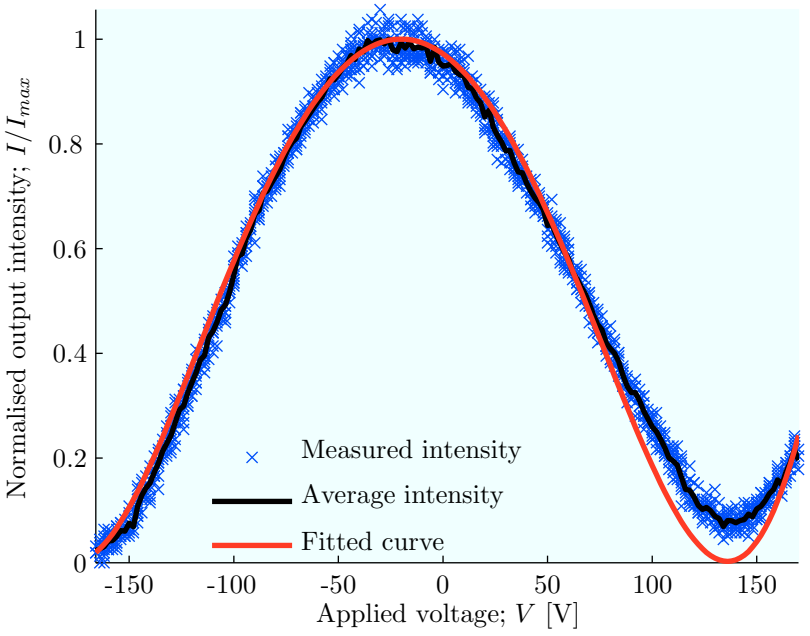


Figure B.7: Curve fitting for device 4, PM7: $\mathfrak{r}_{51} \approx 4.4$ pm/V.

# C Equipment

The equipment listed in table 9 and table 10 was used for this project. The equipment was located at the Department of Electronics and Telecommunications at NTNU during the first half of 2009.

Table 9: Equipment used for fabrication.

| Type | Manufacturer | Model name |
|---|---|---|
| contact aligner | Karl Suss | MA-56 |
| EBPVD | Pfeiffer | Classic 500 |
| diamond saw | Struer | |
| polishing machine | Allied | MultiPrep + TechPrep |
| step index profiler | Taylor-Hobson | Talystep |

Table 10: Equipment used in experimental setup.

| Type | Manufacturer | Model name |
|---|---|---|
| signal generator 1 | Wavetek | Model 145 |
| signal generator 2 | HP | 33120A |
| voltage amplifier | FLC electronics | A800 |
| laser | Anritsu | GB5A016 |
| laser driver | Newport | Model 505 |
| laser temperature controller | Newport | Model 325 |
| probes | Süss | PH100 |
| fibre polarisation-controller | unknown, generic | |
| tapered fibre | | |
| NIR camera | Xenics | Xeva-FPA-1.7-640 |
| polarisation beam splitter | JDS Uniphase | PBC-CP0711333 |
| IR detector | unknown InGaAs-PIN | |
| signal amplifier | no-name, custom | |
| oscilloscope | Tektronix | TDS2004B |
| flexure stage | ELLIOT Scientific | MDE881 |

# D MATLAB code listings

The following MATLAB scripts were used to fit measured data to the model for PMs. Some of the "infrastructure code" has been replaced with pseudo code to improve readability.

Listing 1: curve_fit_pm.m

```
clc; clear;

% Estimates
r       = 2*10^-12;           % starting point for r_51; may require
    tweaking
phi     = 1;                  % starting point for phi; may require
    tweaking
G       = 0.88;               % overlap factor
no      = 2.45;
ne      = 2.45 + 0.005;       % 0.005 birefringence
lambda0 = 1.55*10^-6;
L       = 3*10^-3;
d       = 8*10^-6;
Theta   = pi/4;
alpha   = -pi/4;
% Linearity coefficient for neff.
if data is for device 1 or device 3
    CTE = 0.98;
    CTM = 0.92;
elseif data is for device 2
    CTE = 0.92;
    CTM = 0.92;
    d   = 7*10^-6;
elseif data is for device 4
    CTE = 0.92;
    CTM = 0.92;
end
% Manually select Find offset so that the central symmetry

Load dataset and store data in the following arrays:
  rising_in           % Applied voltage for increasing V
  rising_out          % Measured intensity for increasing V
  falling_in          % Applied voltage for decreasing V
  falling_out         % Measured intensity for decreasing V

if rising is best fit
    [ measured_voltage I ] = sort(rising_in);
    measured_intensity     = rising_out(I);
elseif falling is best fit
    [ measured_voltage I ] = sort(falling_in);
    measured_intensity     = falling_out(I);
end
% Assume 100% ideal modulation depth
measured_intensity = measured_intensity - min(measured_intensity);
% Calculate the average intensity at each unique voltage point.
avg_voltage   = unique(measured_voltage);
avg_voltage   = avg_voltage(~isnan(avg_voltage));
avg_intensity = zeros(1, length(avg_voltage));
for i = 1:length(avg_voltage)
    avg_intensity(i) = mean(measured_intensity(measured_voltage ==
        avg_voltage(i)));
end
```

```
% Fix some strange problems
avg_intensity(isnan(avg_intensity)) = 0;
%avg_intensity = avg_intensity - 0.85*min(avg_intensity);
% Re-normalize dataset so that avg_intensity is normalized.
measured_intensity = measured_intensity / max(avg_intensity);
avg_intensity      = avg_intensity / max(avg_intensity);



Jin = [ 1/sqrt(2); 1/sqrt(2) ];

os  = optimset('TolFun', 10, 'MaxFunEvals', 1000000);
Y   = fminsearch(@(X) fitfun_pm(avg_intensity, avg_voltage+offset, d,
    G, X(1), no, ne-no, L, lambda0, alpha, Theta, X(2), CTE, CTM), ...
                [ r phi ]);

% Result of curve fitting
r     = Y(1)
phi   = Y(2)

Plot fitted curve
```

Listing 2: fitfun_pm.m

```
function err = fitfun_pm(signal, V, d, G, r, no, deltan, L, lambda0,
    alpha, Theta, phi, CTE, CTM)
    I   = iout_calc_pm(V, d, G, r, no, deltan, L, lambda0, alpha,
        Theta, phi, CTE, CTM);
    I   = I / max(I);
    err = norm(I - signal);
end
```

Listing 3: iout_calc_pm.m

```
function Iout = iout_calc_pm(V, d, G, r, no, deltan, L, lambda0,
    alpha, Theta, phi, CTE, CTM)
    Ftantheta = @(V, d, G, r, ne, no) d./(2.*r.*V.*G) .* (1/(ne^2) -
        1/(no^2) + sqrt((1/(no^2) - 1/(ne^2))^2 +
        4.*(r.*G.*V./d).^2));
    Fn1p      = @(V, d, G, r, ne, no, tantheta, CTE, CTM)
        CTE./sqrt(1/(no^2) + r.*V.*G.*tantheta./d);
    Fn3p      = @(V, d, G, r, ne, no, tantheta, CTE, CTM)
        CTM./sqrt(1/(ne^2) - r.*V.*G.*tantheta./d);

    Jin = [ cos(alpha); 1*sin(alpha) ];
    Iout = zeros(1, length(V));
    ne   = no + deltan;

    tantheta                  = Ftantheta(V, d, G, r, ne, no);
    tantheta(isnan(tantheta)) = tan(pi/2);
    theta                     = atan(tantheta);
    theta(isnan(theta))       = pi/2;
    phixp                     = Fn1p(V, d, G, r, ne, no, tantheta,
        CTE, CTM).*L.*2.*pi./lambda0;
    phizp                     = Fn3p(V, d, G, r, ne, no, tantheta,
        CTE, CTM).*L.*2.*pi./lambda0;
    Gr                        = phixp - phizp;

    LPx = [ 1 0; 0 0 ];
        % Linear polariser
```

```
    TR  = @(Gr) [ 1 0; 0 exp(-1i*Gr) ];
        % Wave retarder
    R   = @(theta) [ cos(theta) sin(theta); -sin(theta) cos(theta) ];
        % Coordinate transform

    for j = 1:length(V)
        Jout = R(Theta)*LPx*R(-Theta)*TR(phi) ...
                *R(theta(j))*TR(Gr(j))*R(-theta(j))*Jin;
        Iout(j) = Jout'*Jout;
    end
    % Fix missing values at center.
    center = V == 0;
    Iout(center) = Iout(find(V == 0)+1);
    Iout = Iout./max(Iout);
end
```

# References


[1] G. H. Haertling and C. E. Land. Hot-Pressed (Pb,La)(Zr,Ti)$O_3$ Ferroelectric Ceramics for Electrooptic Applications. *Journal of the American Ceramic Society*, 54:1–11, January 1971.

[2] Ørnulf Nordseth, Thomas Tybell, Jostein K. Grepstad, and Arne Røyset. Sputter-deposited (Pb,La)(Zr,Ti)$O_3$ thin films: Effect of substrate and optical properties. *Journal of Vacuum Science & Technology A: Vacuum, Surfaces, and Films*, 27(3):548–553, 2009.

[3] B. E. A. Saleh and M. C. Teich. *Fundamentals Of Photonics*. Wiley-Interscience, 2007.

[4] R. C. Alferness. Waveguide electrooptic modulators. *Microwave Theory and Techniques, IEEE Transactions on*, 82(8):1121–1137, Aug 1982.

[5] Venkatraman Gopalan, Kenneth L. Schepler, Volkmar Dierolf, and Ivan Biaggio. *The handbook of photonics*, chapter 6. CRC Press, 2006.

[6] MTI Corporation, Richmond, CA, USA. *MgO datasheet*. `http://www.mtixtl.com/xtlflyers/MgO.doc`, Retrieved 2009.05.06.

[7] K. Zheng, J. Lu, and J. Chu. A Novel Wet Etching Process of Pb(Zr,Ti)$O_3$ Thin Films for Applications in Microelectromechanical System. *Japanese Journal of Applied Physics*, 43:3934–+, June 2004.

[8] JDSU, Milpitas, CA, USA. *PBC series datasheet*. `http://www.jdsu.com/product-literature/10113911_003_101305_pbc_ds_cc_ae.pdf`, Retrieved 2009.06.10.

[9] M. Ishii, K. Satoh, M. Kato, and K. Kurihara. Optical properties of epitaxial plzt thin films fabricated by a sol-gel method. pages 77–80, Aug. 2004.

[10] K. Uchiyama, T. Shiosaki, T. Kosaka, A. Kasamatsu, and M. Echizen. Novel electro-optic properties of epitaxially grown (Pb, La)(Zr, Ti)$O_3$ (PLZT) thin films derived by advanced sol-gel methods. *Ceramics International*, 34(4):979 – 983, 2008. The Fifth Asian Meeting on Electroceramics (AMEC-5), The Fifth Asian Meeting on Electroceramics.

[11] Ronald E. Cohen. Origin of ferroelectricity in perovskite oxides. *Letters To Nature*, 358:136–138, 1992.

[12] Venkatraman Gopalan and Rishi Raj. Electric field induced domain rearrangement in potassium niobate thin films studied by in situ second harmonic generation measurements. *Journal of Applied Physics*, 81(2):865–875, 1997.

[13] B. H. Hoerman. *Investigation of the electro-optic and dielectric properties of epitaxial ferroelectric thin films*. PhD thesis, NORTHWESTERN UNIVERSITY, 2001. http://adsabs.harvard.edu/abs/2001PhDT.....45H.